Exploring sources of variation in thermoluminescence emissions and anomalous fading in alkali feldspars

RIEDESEL, S., BELL, Anthony <http://orcid.org/0000-0001-5038-5621>, DULLER, G.A.T., FINCH, A.A., JAIN, M., KING, G.E., PEARCE, N.J. and ROBERTS, H.M.

Published version

Copyright and re-use policy

1 **Exploring sources of variation in thermoluminescence emissions and anomalous fading in alkali**

2 **feldspars**

3

4 S. Riedesel[1], A.M.T. Bell[2], G.A.T. Duller[1], A.A. Finch[3], M. Jain[4], G.E. King[5], N.J. Pearce[1], H. M. Roberts[1]

5

6 [1]Department of Geography and Earth Sciences, Aberystwyth University, United Kingdom

7 [2]Materials and Engineering Research Institute, Faculty of Science, Technology and Arts, Sheffield Hallam
8 University, United Kingdom

9 [3]School of Earth and Environmental Sciences, University of St. Andrews, St. Andrews, United Kingdom

10 [4]Department of Physics, Technical University of Denmark, DTU Risø Campus, Roskilde, Denmark

11 [5]Institute of Earth Surface Dynamics, University of Lausanne, Lausanne, Switzerland

12

13 **Highlights**

14 - TL emission spectra dependent on mineral phases, framework disorder and interfaces

15 - Single-phase feldspars show little anomalous fading

16 - Framework disorder increases intensity of blue TL emission and IRSL fading rate

17

18 **Abstract**

19 Alkali feldspar is routinely used in retrospective dosimetry using luminescence methods. However

20 there is a signal loss over time, termed 'anomalous fading', which results in age underestimation if

21 uncorrected. Although significant improvements have been made in recent years, luminescence

22 dating of feldspars remains challenging. This paper investigates the relationships between chemistry,

23 structural state and the scale of exsolution with thermoluminescence (TL) emission spectra and

24 infrared stimulated luminescence (IRSL) fading rates.

25   We measure TL emission spectra, where possible linking the recombination site to physical features

26   of the feldspar crystals. We show that fading rates are lowest in ordered end-member Na- and K-

27   feldspars but significantly greater in disordered end-members, showing that Al-Si order influences

28   fading. As well as having very low fading rates, ordered end-member samples have distinctive TL

29   emission spectra, with the yellow-green emission dominant, while all other samples have a dominant

30   blue emission. Perthite, i.e. exsolved members of the (Na,K)-feldspar solid solution, show greater

31   fading than disordered end-members and fading is greatest in semi-coherent macroperthite. We

32   propose that the state of Al-Si-order, and the occurrence of defects and dislocations at the perthite

33   lamellar interfaces influence anomalous fading rates in feldspar.

34   **Keywords**

35   Alkali feldspar, thermoluminescence, emission spectra, fading rate, framework disorder

36   **1 Introduction**

37   Luminescence dating of feldspars is routinely conducted using the infrared stimulated luminescence

38   (IRSL) signal and by measuring the emission in the blue (~410 nm) (e.g. Buylaert et al., 2012; Reimann

39   et al., 2012; Smedley et al., 2016; Riedesel et al., 2018). However, feldspar IRSL dating has a major

40   limitation, because it suffers from a signal loss at ambient temperatures, termed anomalous fading

41   (Wintle, 1973; Visocekas, 1985), which results in age underestimation if uncorrected. A range of

42   correction methods has been developed (e.g. Huntley and Lamothe, 2001; Kars et al., 2008), but these

43   often result in large uncertainties on the final age. To circumvent the issues associated with having to

44   quantify and try to correct for fading, research over the past decade has focussed on the isolation of

45   an IRSL signal from feldspar that minimises anomalous fading. Lower fading rates have been obtained

46   by increasing the stimulation temperature (Thomsen et al., 2008) and reduced further by using the

47   signal arising from a second IR stimulation at elevated temperature (termed post-infrared infrared

48   stimulated luminescence signal, post-IR IRSL, e.g. Thomsen et al., 2008; Thiel et al., 2011; Buylaert et

49   al., 2012), or by using a series of IR stimulations at increasing temperatures (termed multiple-elevated-

50   temperature protocols, MET, e.g. Li and Li, 2011).

51   The cause of anomalous fading has been debated for more than 40 years (e.g. Wintle, 1977; Templer,

52   1986; Sanderson, 1988; Visocekas et al., 2014) and a loss of charge from electron traps over time, due

53   to quantum mechanical tunnelling, is the most widely accepted explanation (e.g. Visocekas, 1985).

54   The rate of anomalous fading has been linked to the density of available recombination centres

55   (Huntley, 2006) and significant variations in the rate of fading have been observed in single-crystal

56   feldspars (e.g. Spooner, 1992, 1994; Huntley and Lian, 2006) and in feldspar (single) grains extracted

57   from sediments and bedrock (e.g. Neudorf et al., 2012; Trauerstein et al., 2012; Valla et al., 2016).

58   Visocekas and Zink (1995) measured tunnelling afterglow in microcline and sanidine feldspars and

59   inferred that increased anomalous fading of volcanic feldspars arises due to large concentrations of

60   defects in the crystal caused by Al^{3+} and Si^{4+} disorder on the framework, and additionally due to the

61   inclusion of Fe^{3+} on tetrahedral sites. Based on this observation, Visocekas and Zink (1995) suggested

62   that ordered feldspars, such as microcline, could be dated, because their ordered structure would

63   prevent fading. Indeed, Spooner (1994) observed a stable IRSL signal with the emission recorded

64   between ~330 nm and ~630 nm (using 2 mm Schott BG39 filter) for one of his microcline feldspars and

65   also for an Amelia albite specimen. In contrast, Huntley and Lian (2006) measured IRSL fading rates of

66   the ~360 to ~620 nm emission (using BG39 and Kopp 4-97 filters) of up to 12 % in feldspars that they

67   describe as microclines.

68   However, in most studies the samples are only characterised by their chemical composition, and

69   although a description, which includes the structural state of the feldspar is often included

70   (terminologies such as microcline or sanidine), no data are shown that proves this association. Thus it

71   is difficult to compare fading rates measured with any other mineralogical property of the samples

72   other than the chemical composition. Anomalous fading has often been observed and associated with

73   the volcanic origin of the samples (e.g. Wintle, 1973; Visocekas and Zink, 1995, 1999; Guérin and

74 Visocekas, 2015). However, few fading feldspars used in luminescence dating are of volcanic origin

75 (e.g. Valla et al., 2016; King et al., 2016; Jenkins et al., 2018).

76 Due to exsolution in alkali feldspars during slow cooling in plutonic rocks, such as granite, feldspars

77 are often perthitic (e.g. Parsons et al., 2015). A relationship between interfaces in perthites and the

78 intensity of the UV emission (~290 nm) has been found (Garcia-Guinea et al., 1996). Baril (2004)

79 observed phase-dependent variations of violet and yellow luminescence emissions in perthites, and

80 Correcher et al. (2000) linked the blue luminescence in feldspars with alkali self-diffusion along

81 interfaces offset by hole centres. Spooner (1992) observed variable fading in his feldspars, which

82 contain Na and K. However, no clear relationship between exsolution features and anomalous fading

83 rates has yet been established. Additionally, earlier studies often analysed the IRSL signal of feldspars

84 with a wide emission range (e.g. Spooner, 1992, 1994; Visocekas and Zink, 1999; Huntley and Lian,

85 2006), likely including emissions arising from different defect types (cf. Krbetschek et al. (1997) for a

86 review on emission centres and associated crystal defects in feldspars). Developments within the last

87 decade have changed measurement protocols (e.g. Thomsen et al., 2008; Li and Li, 2011) and a wide

88 range of available optical filters enables the isolation of a narrow emission window, which allows a

89 specific emission to be selected. Thus, there is the need for a re-investigation of potential causes of

90 anomalous fading of the blue IRSL signal in chemically and structurally different feldspars.

91 This paper investigates the links between the blue luminescence emission, the anomalous fading rate

92 of the blue IRSL signal and multiple mineralogical characteristics in alkali feldspars. It explores

93 temperature- and wavelength-resolved variations in the blue luminescence intensity and variations in

94 anomalous fading rates of 12 single-crystal alkali feldspars, and three feldspar grain mixtures extracted

95 from bedrock and sediment. This suite of samples enables the investigation of potential relationships

96 between variations seen in the intensity and anomalous fading rate of the blue luminescence emission

97 and (i) the chemistry of the samples, (ii) the number of phases present in a single crystal specimen (i.e.

98 whether they are single phase or perthitic) and (iii) the degree of framework disorder of the samples.

99

2 Brief overview of the chemistry and structure of feldspars

The crystal lattice of feldspar is made up of $(Al,Si)O_4$ tetrahedra, each connected to four others by shared or "bridging" oxygen ions at their vertices, forming a continuous, interconnected framework. There are four tetrahedral positions within the framework (two of each of the so-called T_1 and T_2-sites), which are occupied by Si^{4+} or Al^{3+}. The framework has a net negative charge, which is offset by large cations (predominantly Na^+, K^+, Ca^{2+}) occupying cavities in the framework termed M-sites (Deer et al., 2013). The compositional variability of most feldspars is accommodated by three end members, each with a different M-site cation: $KAlSi_3O_8$ (K-feldspar), $NaAlSi_3O_8$ (Na-feldspar) and $CaAl_2Si_2O_8$ (Ca-feldspar). The solid solution between K- and Na-feldspars produces the alkali feldspar series; the solid solution between Na- and Ca-feldspar is termed plagioclase. There is very limited solid solution between K- and Ca-feldspar (<10 %). At high temperature (> 1000 °C), complete solid solution across the plagioclase and alkali feldspar series occurs (see Parsons 2010).

Here we consider the alkali feldspar solid solution series between K- and Na-feldspar. The structural state of alkali feldspar is an important indicator of the temperature of crystallisation and subsequent thermal history (Deer et al., 2013) and hence alkali feldspar is divided broadly into low- and high-temperature members. The structural state of low- and high-temperature alkali feldspars is dictated by the degree of ordering of Al and Si within the framework and, in the case of albite (Na-feldspar), coupled with displacive distortions to the framework. Ordered feldspar is equilibrated at low (e.g. <300°C) temperatures. Generally, increased ordering of Al and Si within the framework takes place during slow cooling, e.g. in plutonic rocks. During rapid cooling a disordered distribution of Al and Si at high temperatures is quenched (e.g. sanidine, the monoclinic K-feldspar in volcanic rocks) (Deer et al., 2013).

The progressive ordering in alkali feldspars can be understood in terms of the distribution of Al^{3+} on the framework. In the high-temperature K-feldspar (monoclinic high sanidine), Al^{3+} has an equal (25 %)

124   chance of occupying any of the four tetrahedral sites ($T_1(0)$, $T_1(m)$, $T_2(0)$ and $T_2(m)$) within the more

125   open alkali feldspar framework. During slow cooling, as the framework contracts, Al^{3+} diffuses to

126   occupy preferentially one of the two T_1-sites (giving the monoclinic low sanidine). With continued

127   slow-cooling, Al^{3+} preferentially diffuses into one of the T_1-sites ($T_1(0)$, see Parsons 2010), causing a

128   change in symmetry from monoclinic (sanidine, with the greatest disorder) to triclinic, the ordered K-

129   feldspar maximum microcline (Deer et al., 2013). Associated with this drop in symmetry, microcline

130   adopts repeated twinning in two different orientations visible in a polarising microscope, termed

131   'tartan' or 'tweed' twinning (Deer et al., 2013).

132   Although alkali feldspar is a continuous solid solution at high temperature, the small ionic radius of

133   Na^+ (0.118 nm) triggers a displacive collapse of the framework around Na^+ as the structure attempts

134   to maintain bonding to the smaller Na^+ ion. The feldspar framework cannot collapse around the larger

135   K^+ ion (0.151 nm), hence the alkali feldspar solid solution becomes unstable on cooling and unmixing

136   ('exsolution') of the K- and Na-rich phases in alkali feldspar occurs. Such alkali feldspars are single

137   crystals comprising intergrowths of separate K- and Na-rich feldspars, termed 'perthite'; perthites are

138   further divided into crypto-, micro- and macroperthite, dependent on the scale of the intergrowths

139   (from sub-optical, nanometre scale cryptoperthite, microperthite with lamellae visible under a

140   petrographic microscope, and macroperthite whose lamellae are visible to the naked eye). The cooling

141   rate and fluid interaction after crystallisation of the magma influence the size of the perthite lamellae,

142   with cryptoperthite forming earlier in cooling (Brown and Parsons, 1984a) and coarsening over time.

143   Fluid interaction is involved in the coarsening process of micro- and macro-perthite (e.g. Parsons,

144   1978). Near-pure Na and K feldspars may occur in a variety of environments including deep, high

145   pressure (>0.5 GPa) or high-water content crystallisation of granites/pegmatites (including samples

146   used here e.g. from Minas Gerais, Brazil, CLBR, Table 1, Cassedanne and Roditi, 1996) or wet (low-

147   intermediate grade) metamorphic settings (e.g. albite Al-I, Table 1, Govindaraju, 1995). In these cases,

148   the alkali-feldspar phase relationships during various combinations of slow-cooling, water content and

149   magma/protolith composition can produce almost pure end-member ordered alkali feldspars (see

150 Deer et al., 2013, Parsons, 1978; Parsons et al., 2005). The homogeneity of samples from some of

151 these "exotic" environments (e.g. pegmatites) mean that such pure end-member samples are often

152 used as reference materials or samples for experimentation.

153

154

155 **3 Material and methods**

156 **3.1 Samples**

157 The samples used in this study can be split into two groups, single crystal feldspar specimens and

158 examples of feldspars routinely used for sediment dating and luminescence thermochronometry. The

159 chemical composition of the samples and the mineral phases present were determined by X-ray

160 fluorescence (XRF) and X-ray diffraction (XRD), respectively. Additionally, the samples were examined

161 optically for their colour and the coarseness of any perthite lamella that may be present. We combined

162 our visual inspection, following the definition of perthite microstructures by Deer et al. (2013, p. 253),

163 and the results of the semi-quantitative phase analyses using XRD to separate the perthitic samples

164 into two groups: Both groups have in common that they were determined to be two-phase using XRD.

165 One group of perthites has K- and Na-feldspar lamellae on the optical scale, so that we were able to

166 identify them by eye or using a hand lens. We refer to these feldspar samples as macroperthite. The

167 second group consists of perthite where XRD results defined them as two-phase, but where we were

168 unable to see the lamellae with the naked eye or even through an optical microscope. We refer to

169 these feldspars as cryptoperthite.

170 The chemical composition of the samples was determined by XRF. For XRF measurements 2 g of

171 cellulose binder was placed into an Al sample boat. Powdered sample (0.1 g) was then mixed with

172 cellulose binder (0.1 g) and this mixture was spread on top of the cellulose binder in the Al sample

173 boat. Each boat was then pressed at 20 t to pellets for XRF measurements using a PANalytical MagiX

174   PRO XRF spectrometer equipped with a Rh anode X-ray source. The spectra were collected over ten

175   different energy ranges and then analysed to obtain semi-quantitative results. For the analyses, it was

176   assumed that all elements, except for Cl, were present as oxides. The chemical composition of all

177   samples is summarised in Table S1. Individual sample compositions were calculated to give the

178   molecular formula of the feldspar based on eight oxygen, following stoichiometry. The results are

179   shown in Figure 1A and given in Table 1.

180   Semi-quantitative phase analysis results of the samples were obtained using XRD. The measurements

181   were carried out using a PANalytical X'Pert MPD powder diffractometer operating with Cu Kα X-rays

182   and a PIXCEL-1D area detector. For these measurements 0.1 g of powdered sample was mounted on

183   a low-background silicon XRD sample holder using acetone. Data were collected over the range of 5-

184   100 degrees 2θ, each scan took just over 1 hour.

185   Because of the limited availability of sample material for samples R1-11A and CLBR, and since very

186   detailed characterisation is already published, detailed XRF and XRD measurements were not

187   performed. The chemistry and mineralogy of R1-11A was investigated in detail by Harrison et al.

188   (1990) and the results from their study are used here and are presented in Table 1. The chemical

189   composition determined by Harrison et al. (1990) is based on electron probe microanalyses. Rendell

190   and Clarke (1997) and Garcia-Guinea et al. (1999) performed luminescence experiments and

191   mineralogical investigations of CLBR and determined its structural state as low albite. Additionally,

192   Riedesel et al. (2019) assessed its chemical composition using an XRF detection head attached to a

193   Risø TL/OSL reader (Kook et al., 2012; and see the supplementary material of Stevens et al., 2018). For

194   this measurement a shard of the sample (~1 mm diameter) was placed on a Mo cup (without silicone

195   spray) and the chemical composition was measured three times. The result of this measurement

196   procedure is given, alongside the chemistry of the other samples, in Table 1.

197   Details regarding the origin of the samples, their chemical composition and mineralogical properties

198   as determined using the analyses described above are given in Table 1 for the single crystal specimens,

8

199   and in Table 2 for bedrock and sediment extracts. Single-phase feldspars included in the sample suite

200   are single-phase microcline (FSM-13), and single-phase albite (CLBR and Al-I). Note that Al-I includes

201   5 % quartz, based on semi-quantitative XRD measurements. Photoluminescence and excitation

202   spectra of CLBR were presented by Riedesel et al. (2019, referred to as Cleavelandite).

203   FSM-5 and FSM-11 are macroperthite, with the perthite lamellae visible with the naked eye. Based on

204   semi-quantitative phase analyses using XRD the phases present in these two samples are albite and

205   microcline. Cryptoperthite are R1-11, FSM-3, FSM-7, FSM-8 FSM-14 and FSM-15. The perthite phases

206   are microcline and albite in the case of R1-11A, FSM-3, FSM-7, FSM-8, FSM-14 and FSM-15, and

207   orthoclase and albite for FSM-6, as determined using XRD. Photoluminescence, excitation spectra and

208   cathodoluminescence of R1-11A were presented by Riedesel et al. (2019) and Finch and Klein (1999).

209   WHB-7, the density separated feldspar extract from unconsolidated sediment, consists of microcline

210   and albite, but XRD also showed the presence of muscovite and quartz. HAM-5, another feldspar

211   extract from sediment, consists of orthoclase, albite, quartz and illite, based on semi-quantitative XRD

212   results. The thermochronometry sample MBT-I-2430 consists of feldspar only, in this case microcline

213   and albite. Excitation spectra of HAM-5 and MBT-I-2430 were presented by Riedesel et al. (2019).

214   Whilst all these samples allow us to investigate the influence of differences in the chemical

215   composition and the mineral phases, laboratory heating experiments on FSM-6 and FSM-13 were

216   conducted to enable the investigation of potential effects of framework disorder on the luminescence

217   emissions and fading rates.

218   To explore the effect of Si and Al disorder on luminescence properties, 0.5 g of powdered sample

219   material of samples FSM-6 and FSM-13 (referred to as FSM-6LH and FSM-13LH after heating) were

220   placed in acid cleaned Pt crucibles and heated to 105 °C overnight to remove any potential liquid

221   present in the sample material. The Pt crucibles with the sample material were then placed in a

222   preheated furnace at 1050 °C and covered with fitted Pt lids. The samples remained in the furnace at

223   1050 °C for 5 days (FSM-6LH) and 10 days (FSM-13LH) to allow disordering of Si and Al on the

224 framework. To keep the disordered structure, the samples were rapidly cooled by placing the Pt

225 crucibles in cooled sample holders. Comparison of X-ray diffraction patterns of the unheated and

226 heated material of samples FSM-13/FSM-13LH and FSM-6/FSM-6LH reveals differences linked to

227 states of Al-Si order (Fig. 1B, C). The (131) diffraction peak indicates the triclinicity of the material (a

228 narrow single peak if the sample is triclinic, two peaks if the sample is monoclinic, e.g. Garcia-Guinea

229 et al., 1999). Firstly, Figure 1B and C indicate different degrees of disorder of the two starting materials

230 of FSM-13 and FSM-6 in their X-ray diffraction pattern. Whilst the XRD pattern of FSM-13 shows two

231 fully defined diffraction peaks (131 and 1$\bar{3}$1) between 29° and 32° 2θ, FSM-6 shows only a single peak

232 (131) at 29.8° 2θ with a minor peak (1$\bar{3}$1) around 30° 2θ. This supports results from semi-quantitative

233 phase analyses, based on which FSM-13 was defined as microcline and FSM-6 as two-phase consisting

234 of albite and orthoclase (Table 1). Samples described as orthoclase are microcline with incomplete

235 order of Al^{3+} on T$_1$-sites (Deer et al., 2013, p. 256-257) Secondly, as a result of the heating experiment,

236 the two individual peaks in the diffractogram of FSM-13 (Fig. 1B) move closer together (see red line)

237 and the minor diffraction peak in the diffraction pattern of FSM-6 (Fig. 1C) disappears and only a single

238 diffraction peak around 30° 2θ is visible after heating (FSM-6LH, Fig. 1C, red line). This shows that the

239 heating experiment is successful in disordering both samples, but that the heated material of FSM-

240 6LH is relatively more disordered compared to FSM-13LH.

241 In addition to changes of tetrahedral site occupancy by Al^{3+}, prolonged heating is expected to influence

242 the distribution of K$^+$ and Na$^+$ ions within the perthitic sample FSM-6. Whilst semi-quantitative phase

243 analyses of the unheated sample FSM-6 characterised it as two-phase, with albite and orthoclase as

244 the phases present, the heated sample FSM-6LH is defined as sanidine by XRD, where Na$^+$ and K$^+$ ions

245 are distributed randomly throughout the crystal and not separated in perthite lamellae of K- and Na-

246 feldspar. This becomes apparent when comparing the position of the ($\bar{2}$01) diffraction peak (Deer et

247 al., 2013, p. 260). In the X-ray diffraction pattern of perthitic sample FSM-6 are two ($\bar{2}$01) peaks, one

248 for each phase (at 20.98° 2θ for the microcline phase, at 22.01° 2θ for the albite phase). In contrast,

249 there is only a single ($\bar{2}$01) diffraction peak in FSM-6LH at 21.25° 2θ (Fig. 1D).

250   We also attempted Rietveld refinement, to refine the crystal structure and to quantify the tetrahedral

251   site occupancy by Al^{3+} and Si^{4+} ions. However, due to a strong preferred orientation of the sample

252   material a quantification of the tetrahedral site occupancy was not possible. When using XRD in this

253   manner, we recognise that XRD is a measure of long-range tetrahedral site order (i.e. the development

254   of large, e.g. 100s nm, ordered domains) and relatively insensitive to local short-range order which is

255   better explored by local probes such as Nuclear Magnetic Resonance (NMR, Xiao et al. 1995).

256

257   **3.2 TL emission spectra**

258   Thermoluminescence (TL) emission spectra were measured using an Andor spectrometer (Prasad,

259   2017) attached to a Risø DA20 TL/OSL reader equipped with a $^{90}Sr/^{90}Y$ beta source delivering ~0.1 Gy/s

260   at the sample position and a DASH (Lapp et al., 2015). The single-photon EMCCD-based spectrograph,

261   used to record the spectra, is attached to the Risø reader via a fibre optic bundle cable. The

262   thermoelectrically cooled EMCCD camera (Andor iXon Ultra 888) has a 1024 x 1024 sensor format and

263   a pixel size of 13 μm. The spectral resolution of the system is 13 nm for all spectra recorded. The TL

264   signal was recorded without any optical filters, to allow the emission spectrum to be recorded in a

265   wide range of wavelengths (~280 to ~720 nm). The grating of the spectrograph was set to 150

266   lines/mm and 500 nm blaze. The resulting spectra consist of 1024 bins, ranging from 280.68 nm to

267   718.94 nm, with a bin width of 0.43 nm. The electron-multiplying gain (EM) varied for individual

268   measurements, dependent on the sample brightness, except for the unheated and heated material of

269   FSM-13/FSM-13LH and FSM-6/FSM-6LH, where the EM gain was kept the same, to allow absolute

270   signal intensity comparisons.

271   For TL spectra measurements, samples were placed on stainless steel cups and were beta irradiated

272   using different doses (ranging from 60 to 1,000 Gy), to yield optimal signal output for the samples

273   analysed. To be able to compare absolute intensities for the unheated and heated material of FSM-13

274   and FSM-13LH as well as FSM-6 and FSM-6LH the same sample mass (10 mg) and irradiation dose

275   were used (400 Gy for FSM-13 and FSM-13LH; 200 Gy for FSM-6 and FSM-6LH). A 1000 s pause was

276   inserted after irradiation to allow potential phosphorescence to decay prior to the TL measurement

277   up to 380 °C (heating rate 1 °C/s). A second TL measurement was performed, immediately after the

278   first and used for background subtraction. Repeat measurements were performed and the impact of

279   changing the size of the given dose was tested, to check for reproducibility. All spectra were corrected

280   for the response of the instrument.

281   **3.3 IRSL fading measurements**

282   Infrared stimulated luminescence (IRSL) fading measurements were performed using Risø DA20

283   TL/OSL readers equipped with $^{90}Sr/^{90}Y$ beta sources delivering ~0.03 Gy/s and ~0.1 Gy/s at the sample

284   position. Sample material was placed on stainless steel cups. Typically, three aliquots per sample were

285   measured.

286   Fading was measured for a signal in response to ~90 Gy using a post-IR$_{50}$IRSL$_{225}$ protocol (Table 3) with

287   a preheat at 250 °C for 60 s. The test dose signal was measured after a beta dose of ~30 Gy. The IRSL$_{50}$

288   and post-IR IRSL$_{225}$ signals were recorded through a combination of a Schott BG39 and a Corning 7-59

289   filter (transmission greater than 10 % from 340 nm to 470 nm) using a UV-sensitive photo-multiplier

290   tube (PMT). To ensure stable heating for the IRSL signal measurements, the sample was held at the

291   measurement temperature for 30 s, prior to switching on the IR LEDs. Due to the high signal intensities

292   of FSM-13LH, a ND 1.0 filter was added to the blue filter combination. Delays between different fading

293   measurements ranged from prompt measurements with delays of ~500 to ~800 s between the end of

294   irradiation and luminescence measurement, depending on the instrument, to at least 1,000,000 s. For

295   both signals investigated, the first 10 s were integrated as a signal, and background corrected by

296   subtracting the signal integrated over the last 20 s of each decay curve. Fading rates, expressed as g-

297   values, were calculated using the Analyst software (Duller, 2015) and all g-values presented are

298   normalised to two days (Huntley and Lamothe, 2001).

299   **4 Results**

300   **4.1 TL emission spectra**

301   TL emission spectra of all samples investigated are recorded in the wavelength range from 280 to

302   720 nm and will thus give insights into recombination centres which emit in this part of the

303   electromagnetic spectrum. The main emissions observed are centred at ~300 nm, ~400 nm, ~550 nm

304   and >700 nm (e.g. Krbetschek 1997). However, the intensity of these emissions and the temperature

305   at which the emissions occur varies between samples. The emission spectra from the samples can be

306   divided into four groups: those from single-phase feldspars, perthite with lamellae visible with the

307   naked eye (macroperthite), perthite with lamellae on the sub-optical scale (cryptoperthite) and

308   feldspar extracted from sediments and bedrock, which may contain grains of numerous, (possibly

309   different) feldspar group minerals.

310   The emission spectra recorded for the single-phase feldspars (FSM-13, Al-I and CLBR, Fig. 2), show

311   their brightest emission around 550 nm. Additionally, all three samples show an emission around

312   ~300 nm. The two albite specimens (CLBR and Al-I) also show an emission in the blue (~400 nm) and

313   sample Al-I a tail of a red emission around ~720 nm. The emissions at ~300 and ~550 nm of FSM-13

314   are most intense at ~100 °C (Fig. 2). The temperatures at which the emissions of Al-I and CLBR show

315   their maximum intensity differ slightly for each emission (Fig. 2). For Al-I, the peak of the red emission

316   occurs at the lowest temperature (~100 °C). This is followed by the relatively weak blue emission

317   around ~150 °C and the UV (~300 nm) and yellow-green emission (~550 nm) peak around ~170 °C (Fig.

318   2). Whilst FSM-13 and Al-I show one TL peak at any given emitting wavelength, CLBR displays a number

319   of TL peaks. The strongest emission for CLBR, the yellow-green, shows a low temperature peak around

320   ~95 °C, a second peak at ~170 °C and a shoulder around ~250 °C. Similar behaviour is also visible for

321   the weaker blue emission around ~400 nm. The UV emission (~300 nm) also emits around ~95 °C and

322   around ~170 °C (Fig. 2).

13

323   Perthite in this study are divided into macroperthite and cryptoperthite. Figure 3 shows the emission

324   spectra for all cryptoperthite used in this study. The emission spectra of these samples commonly

325   share a broad emission ranging from ~350 to ~600 nm. Mostly this emission occurs around ~100 °C

326   (Fig. 3), but R1-11A (Fig. 3B) and FSM-7 (Fig. 3F) also show an emission tail towards higher

327   temperatures, resulting in a minor peak around ~350 °C for the emission centred around ~400 nm

328   (Fig. 3). Additionally, all cryptoperthite show the short wavelength tail of a red emission (~700 nm).

329   This emission is strongest for sample FSM-15 (Fig. 3C), a pinkish cryptoperthite, which contains 0.2

330   wt% Fe (Table S1).

331   The emission spectra of the macroperthite samples FSM-5 and FSM-11 (Fig. 4A and B) are similar to

332   those of the cryptoperthite (Fig. 3), as the emissions of these two samples also occur at low

333   temperature (~100 °C). However, the macroperthite show a stronger red emission, compared to the

334   broad blue to yellow emission, which was observed as being dominant in the majority of the

335   cryptoperthite with the exception of FSM-15 (compare Fig. 3 and 4). All emissions for these two

336   samples exhibit a peak at the same temperature (Fig. 4). Sample FSM-11 contains 0.5 wt% Fe, which

337   is consistent with this dominant red emission, though the XRF data for FSM-5 registers no Fe above

338   the detection limit.

339   Further investigation focuses on the effect of prolonged heating to 1050 °C in a furnace and

340   subsequent rapid cooling on TL emission spectra of single-phase feldspars using samples FSM-6LH and

341   FSM-13LH. Figure 6 shows the TL emission spectra for FSM-13 and FSM-13LH, the latter was artificially

342   disordered through heating and rapid cooling as described in section 2.1. The TL spectrum of FSM-13

343   shows a dominant emission around ~550 nm and a dimmer one around ~300 nm (Fig. 5). A weak blue

344   emission (~400 nm) is also present. The maximum intensity of the TL spectrum of FSM-13 of just over

345   3000 cts/°C/0.4 nm is recorded around ~560 nm and at ~100 °C (Figs. 5A and C). The emission

346   spectrum of FSM-13LH differs from the spectrum of FSM-13. FSM-13LH shows its main emission in the

347   blue region of the spectrum, with a peak emission of over 40,000 cts/°C/0.4 nm around ~150 °C (Fig

348 5B). Additionally, the signal now spreads towards higher temperatures, with the blue emission

349 showing a secondary peak around 350 °C (Fig. 5D). A similar shift towards an emission at higher

350 temperature is observed when comparing the TL emission spectra of FSM-6 and FSM-6LH (Fig. 6).

351 Whilst FSM-6 already emitted in the blue region prior to disordering, the spectrum of disordered FSM-

352 6LH shows intensities in the blue emission twice as large as recorded for its unheated counterpart and

353 a narrowing of the emission peak is also observed (Fig. 6A and B). On the basis of the findings for

354 samples FSM-13LH and FSM-6LH, we observe that disordering results in i) an increase in the intensity

355 of the blue luminescence and ii) a shift of the TL emission peak temperature towards higher

356 temperatures.

357 To relate features observed from TL emission spectroscopy of single crystals to material generally used

358 in luminescence dating or thermochronometry, TL spectra were recorded from feldspar extracts from

359 sediments (WHB-7, Fig. 7A and HAM-5, Fig. 7B) and bedrock (MBT-I-2430, Fig. 7C). The emission

360 spectra of these sand-sized feldspar grain mixtures show similar characteristics to the perthitic

361 samples: TL maxima mainly around ~100 °C, a broad emission ranging from ~350 to ~600 nm, and the

362 tail of the red emission (Fig. 7).

363 **4.2 Fading rates**

364 Fading measurements were performed on all samples using a post-IR$_{50}$IRSL$_{225}$ protocol (Table 3). This

365 protocol is chosen as it enables the measurement of two IRSL signals, one at low temperature (50 °C),

366 and a second IRSL signal measured at elevated temperature (225 °C). The data from all IRSL$_{50}$ fading

367 measurements, shown as L_x/T_x ratios after different delays, are presented in Figures S1 to S4 in the

368 supplementary material. In agreement with results shown by Thomsen et al. (2008), we observe

369 consistently lower fading rates for the post-IR IRSL$_{225}$ signal compared to the fading rates of the IRSL$_{50}$

370 signal of our samples (Table 4). We also observe a proportional relationship between the fading rates

371 obtained for the two IRSL signals (Fig. 8A). Şahiner et al. (2017) have shown that the first IRSL

372 measurement step in a post-IR IRSL or post-IR-MET procedure results in the recombination of

373 electrons with the most proximal recombination centres, implying that fading of this first IRSL

374 measurement can give information on the proximal recombination centres. All g-values (%/decade)

375 presented in the following discussion are those obtained for the $IRSL_{50}$ signal. The average g-value (±

376 1 standard deviation) for each sample is shown as a function of their K-feldspar content in Figure 8B.

377 Single-phase albite (CLBR and Al-I) show the lowest fading amongst this suite of samples for the $IRSL_{50}$

378 signal, resulting in g-values of 0.36 ± 0.60 and 0.58 ± 0.30 %/decade respectively. The other single-

379 phase sample (microcline FSM-13) was unique in giving very variable g-values, and hence nine sub-

380 samples were measured. Five aliquots yielded g-values of less than 1%/decade (n = 5, average value

381 is -0.23 ± 0.76 %/decade), one aliquot gave 1.14 ± 0.72 %/decade, and the three others showed fading

382 rates between 2.00 and 3.12 %/decade. Considering the data together by calculating the average and

383 standard deviation results in a very low g-value but with a high uncertainty (0.93 ± 1.52 %/decade, n

384 = 9). The reason for the variability is not known, but we hypothesise that it is due to small-scale

385 variations of structural state within the sample. Solid solutions of microcline are rarely found in nature

386 and, although this sample was determined as single phase microcline, we cannot exclude perthitic

387 patches or local Al disorder within the sample, which cannot be detected by XRD, but which may

388 influence the fading rates.

389 The second group of samples are perthites. The macroperthites (FSM-5 and FSM-11) exhibit the

390 highest fading rates (8.99 ± 1.82 %/decade, FSM-5, n = 3; and 12.42 ± 1.71 %/decade, FSM-11, n = 3).

391 Cryptoperthite show fading rates ranging from 1.80 ± 0.32 %/decade (FSM-8, n = 3) to 6.72 ± 2.51

392 %/decade (R1-11A, n = 3), but all the values are below those recorded for macroperthite.

393 The effect of framework Al disorder on the fading rate was explored using the artificially disordered

394 samples FSM-6LH and FSM-13LH. Heated sample FSM-6LH showed an increase in fading (4.99 ± 0.20

395 %/decade, n = 3), compared to the unheated material (FSM-6, 2.75 ± 1.47 %/decade, n = 3); similarly,

396 an increase in fading rate is observed for disordered FSM-13LH (3.24 ± 0.16 %/decade (n = 3),

397 compared to 0.93 ± 1.52 %/decade (n = 9) for FSM-13).

398   Fading measurements were also performed on feldspars extracted from sediment and bedrock

399   samples, to allow a comparison to material routinely used in luminescence dating studies. Here the

400   fading rates measured are within the range of those determined for cryptoperthite. $IRSL_{50}$ fading rates

401   for sediment samples WHB-7 and HAM-5 are 3.07 ± 0.74 and 1.86 ± 0.46 %/decade, respectively, while

402   the fading rate for the bedrock sample MBT-I-2430 is 3.28 ± 0.14 %/decade.

403   **5 Discussion**

404   **5.1 Thermoluminescence emissions in chemically and structurally different alkali feldspars**

405   The TL emission spectra reveal significant differences in emission centres for single-phase feldspars in

406   comparison to the perthites, particularly regarding the presence and intensity of the blue emission.

407   Single-phase microcline (FSM-13) and albite (CLBR and Al-I) show little blue emission, compared to a

408   relatively intense yellow-green emission, and additionally, an emission in the UV is present in the TL

409   spectra of these samples (Fig. 2). In contrast, in perthitic feldspars (Fig. 3 and 4) the blue emission is

410   dominant, only surpassed in intensity by the red emission in macroperthite (FSM-5 and FSM-11, Fig.

411   4) and cryptoperthite FSM-15 (0.2 wt% Fe, Fig. 3C). Disordering of samples FSM-13 (single-phase

412   microcline) and FSM-6 (perthite: albite and orthoclase) results in an increase in the blue emission

413   intensity recorded for FSM-13LH and FSM-6LH (Fig. 5 and 6). These results are consistent with the blue

414   emission in alkali feldspars being associated with (dis)-ordering of the framework (Finch and Klein,

415   1999) and with the observed sensitisation of the blue emission due to alkali ion leakage caused by

416   prolonged heating (Garcia-Guinea et al., 1999).

417   The defect giving rise to the blue emission in feldspars has been under investigation since the early

418   1980's and it has been suggested that it arises either due to a hole centre located on an Al-bridging

419   oxygen ion (Al^{3+}-O^{1-}-Al^{3+}, e.g. Speit and Lehmann, 1982a; Finch and Klein, 1999) or (for plagioclase) due

420   to Eu^{2+} substituting for Ca^{2+} on M-sites (Götze et al., 1999). A solution involving the silicate framework

421   is the most likely and in alkali feldspar, where Ca^{2+} concentrations are minor (e.g. Table 1), a hole

422   centre on an Al-bridging O is the most likely explanation and is consistent with the results of the

423   present study. The Al-O-Al bridge will only occur where there is a degree of Al-Si framework disorder

424   and it is hypothesised that it is stabilised at low temperatures by the addition of an electron hole (Speit

425   and Lehmann, 1976; Speit and Lehmann, 1982b, Finch and Klein 1999). This is consistent with the

426   spectra recorded for single-phase albite and microcline (CLBR, Al-I and FSM-13), which show very little

427   blue TL emission (Fig. 2). Artificially induced disorder in the microcline sample FSM-13 enhances the

428   blue emission in FSM-13LH, again supporting a model in which Al disorder is implicated in the blue

429   emission intensity. However, the perthitic feldspars are two-phase mixtures of albite and microcline,

430   both of which are partially ordered (Table 1). All perthitic feldspars investigated here emit in the blue

431   (Fig. 3).

432   Garcia-Guinea et al. (1999) linked the UV emission to twin interfaces in the feldspar end-members.

433   Albite and microcline both have multiple twinning, the result of the inversion from monoclinic to

434   triclinic symmetry during cooling. Supporting this, Polymeris et al. (2013) observed more intense UV

435   TL emission in ordered microcline, compared to disordered sanidine. Microcline shows repeated

436   twinning, whilst sanidine does not (cf. Deer et al., 2013, p. 253). In perthite, the possible interfaces

437   include not only the twins within each component phase, but also the interfaces between the K- and

438   Na-feldspar end-members. According to heating experiments (Garcia-Guinea et al. 1999),

439   luminescence attributed to twins contributes to the UV and part of the broad blue emission in perthite

440   (cf. TL spectra in Fig. 3). This is supported by Correcher et al. (2000), who linked the blue luminescence

441   in feldspars with alkali self-diffusion along interfaces offset by hole centres.

442   Perthitic feldspar FSM-6 shows an emission in the blue region. Prolonged heating of the sample

443   material disordered both the Na- and K-feldspar end members, thereby reducing strain at the

444   interfaces and (if accompanied by Na and K diffusion) creating single-phase alkali feldspar with a

445   sanidine structure (FSM-6LH, Table 1, Fig. 1D). Associated with this heating, we observe that the blue

446   TL shifts towards higher temperatures, the emission band narrows and the signal intensity doubles

447   from 10,000 to 20,000 cts/°C/0.4 nm (Fig. 6). This increase supports the suggestion that disorder of Si

448   and Al is implicated in the intensity of the emission.

449   Whilst the blue emission is absent or weak in single-phase albite and microcline, the yellow-green

450   emission (~550 nm) is a key feature of their spectra (Fig. 2). Interestingly, this emission has been

451   associated with Mn^{2+} substituting for Ca^{2+} on M-sites in plagioclase (e.g. Geake et al., 1971; Telfer and

452   Walker, 1978), but it is also present in microcline sample FSM-13. This microcline sample has no

453   detectable CaO content (Table S1) and hence it is unlikely that the emission around ~550 nm of this

454   sample is related to Mn^{2+}. Based on lifetime measurements of the green-yellow emission in a Na-

455   feldspar sample, Prasad et al. (2016) argued that Mn^{2+} substituting for Ca^{2+} on M-sites cannot explain

456   this emission; its recombination lifetime was too short for spin-forbidden Mn^{2+} transitions. Further

457   work is needed to identify the physical nature of this recombination centre but we concur with the

458   findings of Prasad et al. (2016) that it is inconsistent with Mn^{2+}.

459   **5.2 Fading rates of chemically and structurally different alkali feldspars**

460   Fading rates measured for the $IRSL_{50}$ signal (Table 4, Fig. 8B) of chemically and structurally different

461   alkali feldspars range from 0.36 ± 0.6 %/decade (CLBR, n = 3) to 12.42 ± 1.71 %/decade (FSM-11, n =

462   3). Single-phase feldspars show the least fading, whilst macroperthites (FSM-5 and FSM-11)

463   demonstrate the highest fading rates. Cryptoperthite show a similar fading behaviour to samples

464   extracted from bedrock (MBT-I-2430) and sediment (WHB-7, HAM-5), and the fading rates observed

465   for these, range in between those measured for macroperthite and single-phase feldspars (Table 4,

466   Fig. 8B).

467   The low fading rates of the blue emission of the $IRSL_{50}$ signal for single-phase albite and microcline

468   samples coincide with the relatively low blue luminescence signal intensities of these samples, in

469   comparison to the green-yellow emission (compare Fig. 2, 3 and 4 for five samples as examples).

470   Isolated centres are typically modelled in a manner whereby luminescence intensity and defect

471   concentration are proportional (e.g. Speit and Lehmann, 1976, 1982a; Finch and Klein, 1999). Fading,

472 understood as tunnelling from an electron trap to a nearby recombination centre (e.g. Visocekas,

473 1985), is dependent on the density of recombination centres in the vicinity of the electron trap

474 (Huntley, 2006). We infer that where the density of recombination centres increases, the distance

475 between the electron trap as a donor and the recombination centre as the acceptor of the tunnelling

476 electron will be smaller (Jain et al., 2012). In contrast, fewer blue recombination centres will result not

477 only in lower signal intensities, but reduces the likelihood of a blue recombination centre being within

478 tunnelling distance of an electron trap and lower fading rates will be observed.

479 Heating of samples FSM-13LH and FSM-6LH increases the blue luminescence emission intensity (Figs.

480 5 and 6), which we interpret as an increase in Al-Si disorder, populating Al-O-Al bridges and thus

481 increasing the number of blue luminescence centres. Along with the increase in blue luminescence

482 intensity, the fading rate increases (Table 4, Fig. 8B) from 0.93 ± 1.52 %/decade (FSM-13) to 3.24 ±

483 0.16 %/decade (FSM-13LH) and 2.75 ± 1.47 %/decade (FSM-6) to 4.99 ± 0.20 %/decade (FSM-6LH).

484 Another interesting observation can be made when comparing Lx/Tx values of the unheated and

485 heated samples FSM-13/FSM-13LH and FSM-6/FSM-6LH during the fading measurements (Figs. S1 A,

486 B and S2 G, H). The unheated samples show very variable Lx/Tx values between the different aliquots

487 (for instance ranging from ~2.7 to 4.7 for FSM-13, Fig. S1 A) while the heated aliquots have very

488 consistent values (~2.7 for the prompt measurement of FSM-13LH, Fig. S1 B). It is also intriguing that

489 the Lx/Tx values of the prompt measurement of the heated samples are similar to the long delay Lx/Tx

490 values of the unheated counterparts. We cannot explain these two observations, but they may

491 indicate that prolonged heating influences the luminescence sensitivity of the sample material, in a

492 way which cannot be corrected by the test dose. A further observation based on the unheated and

493 heated sample pairs is that while we observe an increase in fading of the IRSL$_{50}$ signal for the heated

494 samples (FSM-13LH and FSM-6LH) compared with their unheated counterparts (FSM-13 and FSM-6),

495 for the post-IR IRSL$_{225}$ signal there is no significant change in fading (Table 4). We conjecture that this

496 could indicate that prolonged heating increases the density of recombination centres proximal to the

497 electron trap (and this causes the increase in fading of the IRSL$_{50}$ signal and the increase in TL signal

498   intensity), but that the heating does not change our ability to isolate distant recombination centres to

499   select a signal with lower fading rate. The observations described above require further investigation

500   to be able to explain fully their implications.

501   Differences in fading rates are also observed for single-phase feldspars and perthites; the single-phase

502   feldspars (CLBR, Al-I, FSM-13) show little signal loss, whereas perthites fade to varying, but

503   significantly greater degrees. A first order model for the behaviour of a perthite is that its properties

504   are a linear combination of the properties of the two end-members, since it is a physical intergrowth

505   of the two end-member phases. However, this is clearly not the case. We can explain the anomalous

506   behaviour of the intergrowths in two ways: a) the Na- and K-feldspar components of the perthites

507   have greater disorder than the pure end-members or b) that the fading is related to the interfaces

508   between the Na- and K-feldspar components. Hypothesis (a) is credible – we show above that

509   increased disorder promotes fading. Furthermore, the lattice mismatch between Na- and K-feldspars

510   increases as they become more ordered and lattice strain resists ordering (Deer et al., 2013, p. 263-

511   264). Hence end member Na- and K-feldspar samples will have greater Al-Si order than a perthite

512   grown under the same conditions. However, hypothesis (b) is also credible – interfaces are atypical

513   regions which stabilise or destabilise defects and whose states of order may be locally different to the

514   bulk feldspar. Garcia-Guinea et al. (1999) suggested that a component of the blue luminescence is

515   related to twins. Interfaces may stabilise different defect types; two different defects that are unlikely

516   to occur together in a random distribution in the bulk may occur in close proximity on an interface.

517   This suggests that a single-phase solid solution may have different properties from a perthite of the

518   same bulk composition.

519   To explore the two hypotheses a) and b) above, we contrast the behaviour of macroperthite and

520   cryptoperthite. Cryptoperthites have nm-scale intergrowths and there is a greater volume of the

521   feldspar bulk occupied by interface (Brown and Parsons, 1984b). Also, since the elastic interfacial

522   strain in cryptoperthite is so high, one expects the Al-Si disorder to be greater in cryptoperthite

523   compared to a macroperthite of the same composition. However, we observe that macroperthite

524   show greater fading rates than cryptoperthite (Fig 8, Table 4). If the state of order (hypothesis a) were

525   the sole driving factor, the opposite would have been observed. Our conclusion is therefore that the

526   interfaces between the Na- and K-feldspar phases are implicated in the fading of perthite. In

527   cryptoperthite, this may be elastic strain around the interfaces at which the two different feldspar

528   lattices are forced to remain coherent (Brown et al. 1997). Since the fading rates of cryptoperthite and

529   macroperthite are different, we explore the differences in the morphologies of the interfaces.

530   Boundaries between the K- and Na- feldspar phases in cryptoperthite are highly strained but fully

531   coherent (i.e. the framework passes continuously from one phase to another, Brown et al., 1997). In

532   macroperthite, interfaces are semi-coherent, i.e. the lattices are commonly joined across the

533   boundary but not always, creating a region of dislocations and dangling bonds (e.g. Lee et al. 1995,

534   Lee and Parsons, 1997; Parsons et al., 2015). Since fading is understood as the loss of charge from an

535   electron trap to a nearby recombination centre, we hypothesise that a higher density of defects

536   concentrated around semi-coherent interfaces in macroperthite are implicated in the higher fading

537   rates. It may be that defect families such as regions of local disorder, dangling bonds, element

538   substitutions etc. are all stabilised by their proximity to semi-coherent perthite interfaces, driving

539   defects to cluster, which in turn allows direct defect-defect interactions. Interfaces are thus proposed

540   as regions in which high defect densities result in shorter distances between donor and acceptor of a

541   tunnelling electron (Jain et al., 2012).

542   Thus, we propose that fading in feldspars is not only a phenomenon of feldspars with a high-

543   temperature (disordered) structural state, such as volcanic feldspars (e.g. Wintle, 1973; Visocekas and

544   Zink, 1995; Visocekas et al., 2014; Guérin and Visocekas, 2015), but also related to perthite interfaces.

545   Fading is controlled by the density of defects (Huntley, 2006) and defect clustering, which in turn is

546   inferred to be influenced by (i) the degree of Si and Al ordering on the framework, (ii) the interfaces

547   in perthites and (iii) elastic strain areas within the feldspar crystal. The only feldspars in this study,

548   which show fading rates below 1 % are ordered single-phase albite and microcline. This observation

549   of very low fading rates of ordered feldspars is in good agreement with suggestions by Visocekas and

550   Zink (1995) and fading measurements on some microcline and albite specimen by Spooner (1994).

551   Our fading results show that for alkali feldspars, the structural state and the nature of interfaces within

552   the crystal are more important than chemical composition when interpreting luminescence. The

553   observation of increasing fading with increasing Al disorder on the framework is consistent with the

554   properties of plagioclase in which fading rises almost linearly with increasing concentration of Ca^{2+}

555   (Huntley and Lian 2006; Huntley et al. 2007) since Ca^{2+} substitution on the M-site is offset by increases

556   in the Al content of the lattice and therefore Al-O-Al populations are dependent on Ca content.

557   Due to exsolution of feldspar during cooling in plutonic rocks (e.g. granite), most alkali feldspars in

558   rocks and unconsolidated sediments are perthites (e.g. Deer et al., 2013). Unfortunately, perthites

559   faded in our experiments. The feldspars extracted from unconsolidated sediments (WHB-7 and HAM-

560   5) and from crushed bedrock material used in luminescence thermochronometry (MBT-I-2430) in this

561   study exhibit fading rates of the $IRSL_{50}$ signal within the range seen for cryptoperthites in this study

562   (Table 4, Fig. 8B). A similarity in fading rates and in TL emission spectra of sediment and

563   thermochronometry samples and perthite is consistent with similar mechanisms playing a role in

564   these sets of samples. The similarities hint that in feldspar grains extracted from sediment and rocks

565   for optical dating and thermochronometry, Al-Si order, interface morphology and elastic strain are

566   implicated both in the blue emission and in the fading rate.

567   **6 Conclusions**

568   The present study analyses the effects of chemistry, the number of phases present within a single

569   crystal and the relative degree of framework disorder on TL emission spectra and fading rates of alkali

570   feldspars. The investigated sample suite includes Na- and K-feldspar end members, perthites with K-

571   and Na-feldspar lamellae on different scales, as well as material routinely used in luminescence dating

572   studies and luminescence thermochronometry. We observed variations in the intensity of the blue

573   luminescence emission and the rate of anomalous fading of the IRSL signal in our feldspars. We

574 associate the blue luminescence with the blue recombination centre being located on an Al-O-Al

575 bridge. The blue luminescence intensity increases as a function of the population of Al-O-Al bridges

576 which increases with Al-Si disorder. Ordered, single-phase feldspars, such as albite and microcline,

577 show very little fading, whereas the variations in fading rates in perthites are suggested to be linked

578 to a) the degree of Si and Al order on the framework and b) defect clustering associated with semi-

579 coherent perthite interfaces which modify the intensity of the blue emission and the extent to which

580 this emission fades.

581 Our study highlights the importance of detailed mineralogical characterisation of feldspar samples in

582 order to understand the complex drivers behind the variability seen in the blue luminescence intensity

583 and anomalous fading rates of the IRSL signal. This paper combines information on sample chemistry,

584 structural state, phases present, luminescence emissions and anomalous fading rate of alkali feldspar.

585 From these data we are able to differentiate between very low fading single-phase end members and

586 perthitic feldspars which all fade. Interestingly, the same differentiation can be made from TL emission

587 spectra, where single-phase feldspars show a more intense yellow-green emission, compared to the

588 blue emission, while perthites show the opposite, with the blue emission being dominant. Perhaps it

589 would be possible to identify those feldspar grains which are single phase (and hence likely to have a

590 low fading rate) by looking for those with a high value for the ratio of the yellow-green to blue

591 emission. Such measurements could be routinely feasible using automated filter changers in

592 combination with an EMCCD camera, and may avoid the need for costly and time consuming chemical

593 and structural analyses of individual grains.

24

606   **References**

607   Baril, M.R., 2004. CCD imaging of the infra-red stimulated luminescence of feldspar. Radiation

608   Measurements 38, 81-86.

609   Brown, W.L., Parsons, I., 1984a. The nature of potassium feldspar, exsolution microtextures and

610   development of dislocations as a function of composition in perthitic alkali feldspars. Contributions to

611   Mineralogy and Petrology 86, 335-341.

612   Brown, W.L., Parsons, I., 1984b. Exsolution and coarsening mechanisms and kinetics in an ordered

613   cryptoperthites series. Contributions to Mineralogy and Petrology 86, 3-18.

614   Brown, W.L., Lee, M.R., Waldron, K.A., Parsons, I., 1997. Strain-driven disordering of low microcline to

615   low sanidine during partial phase separation in microperthites. Contributions to Mineralogy and

616   Petrology 127, 305-313.

617   Bussy, F., Von Raumer, J.F., 1993. U-Pb dating of Palaeozoic events in the Mont-Blanc crystalline

618   massif, western Alps. Terra. Nova Abstracts 5, 382.

619   Bussy, F., Schaeltegger, U., Marro, C., 1989. The age of the Mont Blanc granite (western Alps): a

620   heterogenous isotopic system dated by Rb-Sr whole rock determination on its microgranular enclaves.

621   Schweizer Mineralogische und Petrologische Mitteilungen 69, 3–13.

622 Buylaert, J.-P., Jain, M., Murray, A.S., Thomsen, K.J., Thiel, C., Sohbati, R., 2012. A robust feldspar

623 luminescence dating method for Middle and Late Pleistocene sediments. Boreas 41, 435-451.

624 Cassadanne, J.P., Roditi, M., 1996. The location, geology and mineralogy of gem tourmalines in Brazil.

625 Journal of Gemmology 25 (4), 263–298.

626 Correcher, V., Garcia-Guinea, J., Delago, A., 2000. Influence of preheating treatment on the

627 luminescence properties of adularia feldspar ($KAlSi_3O_8$). Radiation Measurements 32, 709-715.

628 Cunningham, G.J., 1981. Petrology and geochemistry of Lewisian pegmatites and granites, N.W.,

629 Scotland. PhD thesis, Imperial Collage London, United Kingdom.

630 Deer, W.A., Howie, R.A., Zussman, J., 2013. An introduction to the rock-forming minerals. Third

631 Edition. Mineralogical Society of Great Britain and Ireland.

632 Duller, G.A.T., 2015. The Analyst software package for luminescence data: overview and recent

633 improvements. Ancient TL 33, 35-42.

634 Finch, A.A., Klein, J., 1999. The causes and petrological significance of cathodoluminescence emissions

635 from alkali feldspars. Contributions to Mineralogy and Petrology 135, 234-243.

636 Garcia-Guinea, J., Rendell, H.M., Sanchez-Muñoz, L., 1996. Luminescence spectra of alkali feldspars:

637 some relationships between structural features and luminescence emission. Radiation Protection

638 Dosimetry 66, 395-398.

639 Garcia-Guinea, J., Townsend, P.D., Sanchez-Muños, L.., Rojo, J.M., 1999. Ultraviolet-blue ionic

640 luminescence of alkali feldspars from bulk and interfaces. Physics and Chemistry of Minerals 26, 658-

641 667.

642 Geake, J.E., Walker, G., Mills, A.A., Garlick, G.F.J., 1971. Luminescence of Apollo lunar samples.

643 Proceedings of the Second Lunar Science Conference 3, 2265-2275.

644 Govindaraju, K., 1995. Update (1984-1995) on two GIT-IWG geochemical reference samples: Albite

645 from Italy, Al-I and iron formation sample from Greenland, IF-G. Geostandards Newsletter 19, 55-96.

646 Guérin, G., Visocekas, R., 2015. Volcanic feldspars anomalous fading: Evidence for two different

647 mechanisms. Radiation Measurements 81, 218-223.

648 Harrison, T.N., Parsons, I., Brown, P.E., 1990. Mineralogical evolution of fayalite-bearing rapakivi

649 granites from the Prins Christians Sund pluton, South Greenland. Mineralogical Magazine 54, 57–66.

650 Huntley, D.J., Lamothe, M., 2001. Ubiquity of anomalous fading in K-feldspars and the measurement

651 and correction for it in optical dating. Canadian Journal of Earth Sciences 38, 1093-1106.

652 Huntley, D.J., 2006. An explanation of the power-law decay of luminescence. Journal of Physics:

653 Condensed Matter 18, 1359-1365.

654 Huntley, D.J., Lian, O.B., 2006. Some observations on tunnelling of trapped electrons in feldspars and

655 their implications for optical dating. Quaternary Science Reviews 25, 2503-2512.

656 Huntley, D.J., Baril, M.R., Haider, S., 2007. Tunnelling in plagioclase feldspars. Journal of Physics D:

657 Applied Physics 40, 900-906.

658 Jain, M., Guralnik, B., Andersen, M. T., 2012. Stimulated luminescence emission from localized

659 recombination in randomly distributed defects. Journal of Physics: Condensed Matter 24, 385402.

660 Jenkins, G.T.H., Duller, G.A.T., Roberts, H.M., Chiverrell, R.C., Glasser, N.F., 2018. A new approach for

661 luminescence dating glaciofluvial deposits – High precision optical dating of cobbles. Quaternary

662 Science Reviews 192, 263-273.

663 Kars, R.H., Wallinga, J., Cohen, K.M., 2008. A new approach towards anomalous fading correction for

664 feldspar IRSL dating – tests on samples in field saturation. Radiation Measurements 43, 786-790.

665 King, G.E., Herman, F., Guralnik, B., 2016. Northward migration of the eastern Himalayan syntaxis

666 revealed by OSL thermochronometry. Science 353, 800-804.

667 Kook, M.H., Lapp, T., Murray, A.S., Thiel, C., 2012. A Risø XRF Attachment for Major Element Analysis

668 of Aliquots of Quartz and Feldspar Separates. UK Luminescence and ESR Meeting, Aberystwyth, pp.

669 37 September 2012 (abstract).

670 Krbetschek, M.R., Gütze, J., Dietrich, A., Trautmann, T., 1997. Spectral information from minerals

671 relevant for luminescence dating. Radiation Measurements 27, 695-748.

672 Lapp, T., Kook, M., Murray, A.S., Thomsen, K.J., Buylaert, J.-P., Jain, M., 2015. A new luminescence

673 detection and stimulation head for the Risø TL/OSL reader. Radiation Measurements 81, 178-184.

674 Lee, M.R., Waldron, K.A., Parsons, I., 1995. Exsolution and alteration microtextures in alkali feldspar

675 phenocrysts from the Shap granite. Mineralogical Magazine 59, 63-78.

676 Lee, M.R., Parsons, I., 1997. Dislocation formation and albitization in alkali feldspars from the Shap

677 Granite. Mineralogical Magazine 82, 557-570.

678 Li, B., Li, S.-H., 2011. Thermal stability of infrared stimulated luminescence of sedimentary K-feldspar.

679 Radiation Measurements 46, 29-36.

680 Neudorf, C.M., Roberts, R.G., Jacobs, Z., 2012. Sources of overdispersion in a K-rich feldspar sample

681 from north-central India: Insights from De, K content and IRSL age distributions for individual grains.

682 Radiation Measurements 47, 696-702.

683 Parsons, I., 1978. Feldspars and fluids in cooling plutons. Mineralogical Magazine 42, 1-17.

684 Parsons, I., Thompson, P., Lee, M.R., Cayzer, N., 2005. Alkali feldspar microtextures as provenance

685 indicators in siliclastic rocks and their role in feldspar dissolution during transport and diagenesis.

686 Journal of Sedimentary Research 75, 921-942.

687 Parsons, I., 2010. Feldspars defined and described: a pair of posters published by the Mineralogical

688 Society. Sources and supporting information. Mineralogical Magazine, 74(3), 529-551.

689   Parsons, I., FitzGerald, J.D., Lee, M.R., 2015. Routine characterization and interpretation of complex

690   alkali feldspar intergrowth. American Mineralogist 100, 1277-1303.

691   Polymeris, G.S., Theodosoglou, E., Kitis, G., Tsirliganis, N.C., Koroneos, A., Paraskevopoulos, K.M.,

692   2013. Preliminary results on structural state characterization of K-feldspars by using

693   thermoluminescence. Mediterranean Archaeology and Archaeometry 13, 155-161.

694   Prasad, A.K., Lapp, T., Kook, M., Jain, M., 2016. Probing luminescence centres in Na rich feldspars.

695   Radiation Measurements 90, 292-297.

696   Prasad, A.K., 2017. Understanding defect related luminescence processes in wide bandgap materials

697   using low temperature multi-spectroscopic techniques. PhD Thesis, Technical University of Denmark,

698   196 p.

699   Reimann, T., Thomsen, K.J., Jain, M., Murray, A.S., Frechen, M., 2012. Single-grain dating of young

700   sediments using the pIRIR signal from feldspar. Quaternary Geochronology 11, 28-41.

701   Rendell,   H.M.,   Clarke,   M.L.,   1997.   Thermoluminescence,   radioluminescence   and

702   cathodoluminescence spectra of alkali feldspars. Radiation Measurements 27, 263-272.

703   Riedesel, S., Brill, D., Roberts, H.M., Duller, G.A.T., Garrett, E., Zander, A.M., King, G.E., Tamura, T.,

704   Burow, C., Cunningham, A., Seeliger, M., De Batist, M., Heyvaert, V.M.A., Fujiwara, O., Brückner, H.

705   and the QuakeRecNankai Team, 2018. Single-grain luminescence chronology of historical extreme-

706   wave event deposits recorded in a coastal lowland, Pacific coast of central Japan. Quaternary

707   Geochronology 45, 37–49.

708   Riedesel, S., King, G.E., Prasad, A.K., Kumar, R., Finch, A.A., Jain, M., 2019. Optical determination of

709   the width of the band-tail states, and the excited and ground state energies of the principal dosimetric

710   trap in feldspar. Radiation Measurements 125, 40-51.

711 Şahiner, E., Kitis, G., Pagonis, V., Meriç, N., Polymeris, G.S., 2017. Tunnelling recombination in

712 conventional, post-inrared and post-infrared multi-elevated temperature IRSL signals in microcline

713 feldspar. Journal of Luminescence 188, 514-523.

714 Sanderson, D.C.W., 1988. Fading of thermoluminescence in feldspars: Characteristics and corrections.

715 Nuclear Tracks and Radiation Measurements 14, 155-161.

716 Smedley, R.K., Glasser, N.F., Duller, G.A.T., 2016. Luminescence dating of glacial advances at Lago

717 Buenos Aires (~46°S), Patagonia. Quaternary Science Reviews 134, 59-73.

718 Speit, B., Lehmann, G., 1976. Hole centers in the feldspar sanidine. Physica Status Solidi 36, 471-481.

719 Speit, B., Lehmann, G., 1982a. Radiation Defects in Feldspars. Physics and Chemistry of Minerals 8, 77-

720 82.

721 Speit, B., Lehmann, G., 1982b. A comparative study of thermoluminescence and isothermal

722 destruction of radiation defects in feldspars. Journal of Luminescence 27, 127-136.

723 Spooner, N.A., 1992. Optical dating: Preliminary results on the anomalous fading of luminescence from

724 feldspars. Quaternary Science Reviews 11, 139-145.

725 Spooner, N.A., 1994. The anomalous fading of infrared-stimulated luminescence from feldspars.

726 Radiation Measurements 23, 625-632.

727 Stevens, T., Buylaert, J.-P., Thiel, C., Ujavri, G., Yi, S., Murray, A.S., Frechen, M., 2018. Ice-volume-

728 forced erosion of the Chinese Loess Plateau global Quaternary stratotype site. Nature

729 Communications 9: 983.

730 Telfer, D.J., Walker, G., 1978. Ligand field bands of Mn^{2+} and Fe^{3+} luminescence centres and their site

731 occupancy in plagioclase feldspars. Modern Geology 6, 199-210.

732 Templer, R.H., 1986. The localised transition model of anomalous fading. Radiation Protection

733 Dosimetry 17, 493-497.

734 Thiel, C., Buylaert, J.-P., Murray, A.S., Terhorst, B., Hofer, I., Tsukamoto, S., Frechen, M., 2011.

735 Luminescence dating of the Stratzing loess profile (Austria) – Testing the potential of an elevated

736 temperature post-IR IRSL protocol. Quaternary International 234, 23-31.

737 Thomsen, K.J., Murray, A.S., Jain, M., Bøtter-Jensen, L., 2008. Laboratory fading rates of various

738 luminescence signals from feldspar-rich sediment extracts. Radiation Measurements 43, 1474-1486.

739 Trauerstein, M., Lowick, S., Preusser, F., Rufer, D., Schlunegger, F., 2012. Exploring fading in single

740 grain feldspar IRSL measurements. Quaternary Geochronology 10, 327-333.

741 Ussher, W.A.E., Barrow, G., McAlister, D.A., 1909. The Geology of the country around Bodmin and St.

742 Austell. Memoirs of the Geological Survey England and Wales – Explanation of Sheet 347.

743 Valla, P.G., Lowick, S.E., Herman, F., Champagnac, J.-D., Steer, P., Guralnik, B., 2016. Exploring IRSL50

744 fading variability in bedrock feldspars and implications for OSL thermochronometry. Quaternary

745 Geochronology 36, 55-66.

746 Visocekas, R., 1985. Tunnelling radiative recombination on labradorite: Its association with anomalous

747 fading of thermoluminescence. Nuclear Tracks and Radiation Measurements 10, 521-529.

748 Visocekas, R., Zink, A., 1995. Tunneling afterglow and point defects in feldspars. Radiation Effects and

749 Defects in Solids 134, 265-272.

750 Visocekas, R., Zink, A., 1999. Use of the red TL emission band of alkali feldspars for dosimetry and

751 dating. Quaternary Geochronology 18, 271-278.

752 Visocekas, R., Barthou, C., Blanc, P., 2014. Thermal quenching of far-red Fe^{3+} thermoluminescence of

753 volcanic K-feldspars. Radiation Measurements 61. 52-73.

754 Wintle, A.G., 1973. Anomalous fading of thermoluminescence in mineral samples. Nature 245, 143-

755 144.

756   Wintle, A.G., 1977. Detailed study of a thermoluminescent mineral exhibiting anomalous fading.

757   Journal of Luminescence 15, 385-393.

758   Xiao, Y., Kirkpatrick, J., Hay, R.L., Kim, Y.J., Phillips, B.L., 1995. Investigation of Al,Si order in K-feldspars

759   using ^{27}Al and ^{29}Si MAS NMR. Mineralogical Magazine 59, 47-61.

760

Table 1. Details regarding the origin, chemical composition, phases and size of perthite lamella for samples investigated. The chemical composition in % feldspars, was done using stoichiometric conversion of the semi-quantitative XRF data. Chemical composition and present phases of R1-11A was taken from Harrison et al. (1990). Present phases are based on semi-quantitative XRD analyses.

Sample ID	Origin	Chemical composition (FS %)			Phases						Extent of perthite development	Reference
		K-FS	Na-FS	Ca-FS	Microcline	Orthoclase	Sanidine	Albite	Anorthite	Other		
FSM-13	Brazil	98.5	1.5	0.0	100.0	-	-	-	-	-	none	-
FSM-13LH	Brazil	98.5	1.5	0.0	100.0	-	-	-	-	-	none	-
FSM-3	Granite pegmatite, Toe Head, South Harris, Scotland, UK (Cunningham, 1981)	82.5	17.2	0.3	78.0	-	-	22.0	-	-	cryptoperthites	-
R1-11A	Rapakivi Granite, South Greenland	81.0	19.0	1.0	Microcline and albite (Harrison et al., 1990)						cryptoperthite	Harrison et al., 1990; Finch and Klein, 1999; Riedesel et al., 2019
FSM-15	Buckingham, Quebec, Canada	80.4	19.6	0.0	82.0	-	-	18.0	-	-	cryptoperthite	-
FSM-14	Iveland, Southern Norway	78.3	21.2	0.5	54.0	-	-	46.0	-	-	cryptoperthite	-
FSM-8	Norway	77.1	22.6	0.3	68.0	-	-	32.0	-	-	cryptoperthite	-
FSM-7	Unknown	76.8	22.0	1.2	48.0	-	-	51.0	-	1.0	cryptoperthite	-
FSM-5	Unknown	74.8	25.20	0.0	57.0	-	-	43.0	-	-	Macroperthite	-
FSM-6	Granite pegmatite, Trezaise Quarry, Cornwall, UK (see Ussher et al., 1909)	74.4	25.3	0.3	-	38.0	-	62.0	-	-	cryptoperthite	-
FSM-6LH	Trezaise Quarry, Cornwall, UK	74.4	25.3	0.3	-	-	100.0	-	-	-	none	-
FSM-11	Perth, Canada	65.2	34.8	0.0	62.0	-	-	38.0	-	-	macroperthite	-
Al-I	Pinzele, Trente, Italy (Govindaraju, 1995)	1.0	97.0	2.0	-	-	-	-	-	-	none	-
CLBR	Pegmatite, Golonca District, Minas Gerais, Brazil (Cassadanne and Roditi, 1996)	0.5	99.3	0.2	-	-	-	100	-	-	none	Rendell and Clarke (1997); Garcia-Guinea et al., 1999; Riedesel et al., 2019

Table 2. Details on feldspar extracted from sediment and bedrock samples. The chemical composition in % feldspars, was done using stoichiometric conversion of the semi-quantitative XRF data. Present phases are based on semi-quantitative XRD analyses.

| Sample ID | Origin | Chemical composition (FS %) | | | Phases | | | | | | Size of perthite lamella | Reference |
		K-FS	Na-FS	Ca-FS	Microcline	Orthoclase	Sanidine	Albite	Anorthite	Other		
MBT-I-2430	Calc-alkaline granite, Mont Blanc, Italy (Bussy et al., 1989; Bussy and Von Raumer, 1993)	86.1	13.4	0.6	85.0	-	-	15.0	-	-	-	Lambert, 2018; Riedesel et al., 2019
HAM-5	Lake Hamana, Japan	70.4	27.2	2.4	-	30.0	-	27.0	-	43.0	-	Riedesel et al. 2019
WHB-7	Channelled Scablands, Washington State, USA	63.9	31.5	4.6	37.0	-	-	30.0	-	33.0	-	-

Table 3. Post-IR$_{50}$IRSL$_{225}$ protocol used for the determination of fading rates.

Step	Details	Obtained
1	Beta dose ~90 Gy	
2	Preheat for 60 s at 250 °C	
3	IR stimulation at 50 °C for 200 s (IRSL$_{50}$)	Lx$_1$ (IRSL$_{50}$)
4	IR stimulation at 225 °C for 300 s (post-IR IRSL$_{225}$)	Lx$_2$ (post-IR$_{50}$IRSL$_{225}$)
5	Beta dose ~30 Gy	
6	Preheat for 60 s at 250 °C	
7	IR stimulation at 50 °C for 200 s (IRSL$_{50}$)	Tx$_1$ (IRSL$_{50}$)
8	IR stimulation at 225 °C for 300 s (post-IR IRSL$_{225}$)	Tx$_2$ (post-IR$_{50}$IRSL$_{225}$)

Table 4. Fading rates for the two luminescence signals recorded using a post-IR$_{50}$ IRSL$_{225}$ protocol. The samples were preheated to 250 °C for 60 s, prior to IRSL measurements.

| Group	Sample ID	Fading rate (g2days, %/decade)	
		IRSL$_{50}$	Post-IR IRSL$_{225}$
Single phase			
	Al-I	0.58 ± 0.30	0.29 ± 0.24
	CLBR	0.36 ± 0.60	-0.08 ± 0.37
	FSM-13	0.93 ± 1.52	0.54 ± 1.10
Macroperthites			
	FSM-5	8.99 ± 1.82	2.74 ± 0.60
	FSM-11	12.42 ± 1.71	4.07 ± 1.39
Cryptoperthites			
	FSM-3	5.71 ± 0.12	2.19 ± 0.49
	R1-11A	6.72 ± 2.51	1.86 ± 1.39
	FSM-15	4.97 ± 1.98	0.79 ± 1.73
	FSM-14	3.51 ± 1.35	1.48 ± 1.63
	FSM-8	1.80 ± 0.32	1.23 ± 1.86
	FSM-7	4.13 ± 0.46	0.55 ± 0.38
	FSM-6	2.75 ± 1.47	1.47 ± 0.97
Artificially disordered			
	FSM-13LH	3.24 ± 0.16	-0.06 ± 0.13
	FSM-6LH	4.99 ± 0.20	1.68 ± 0.13
Sediments/rocks			
	HAM-5	1.86 ± 0.46	-1.01 ± 0.20
	WHB-7	3.07 ± 0.74	1.01 ± 0.26
	MBT-I-2430	3.28 ± 0.14	1.35 ± 0.30
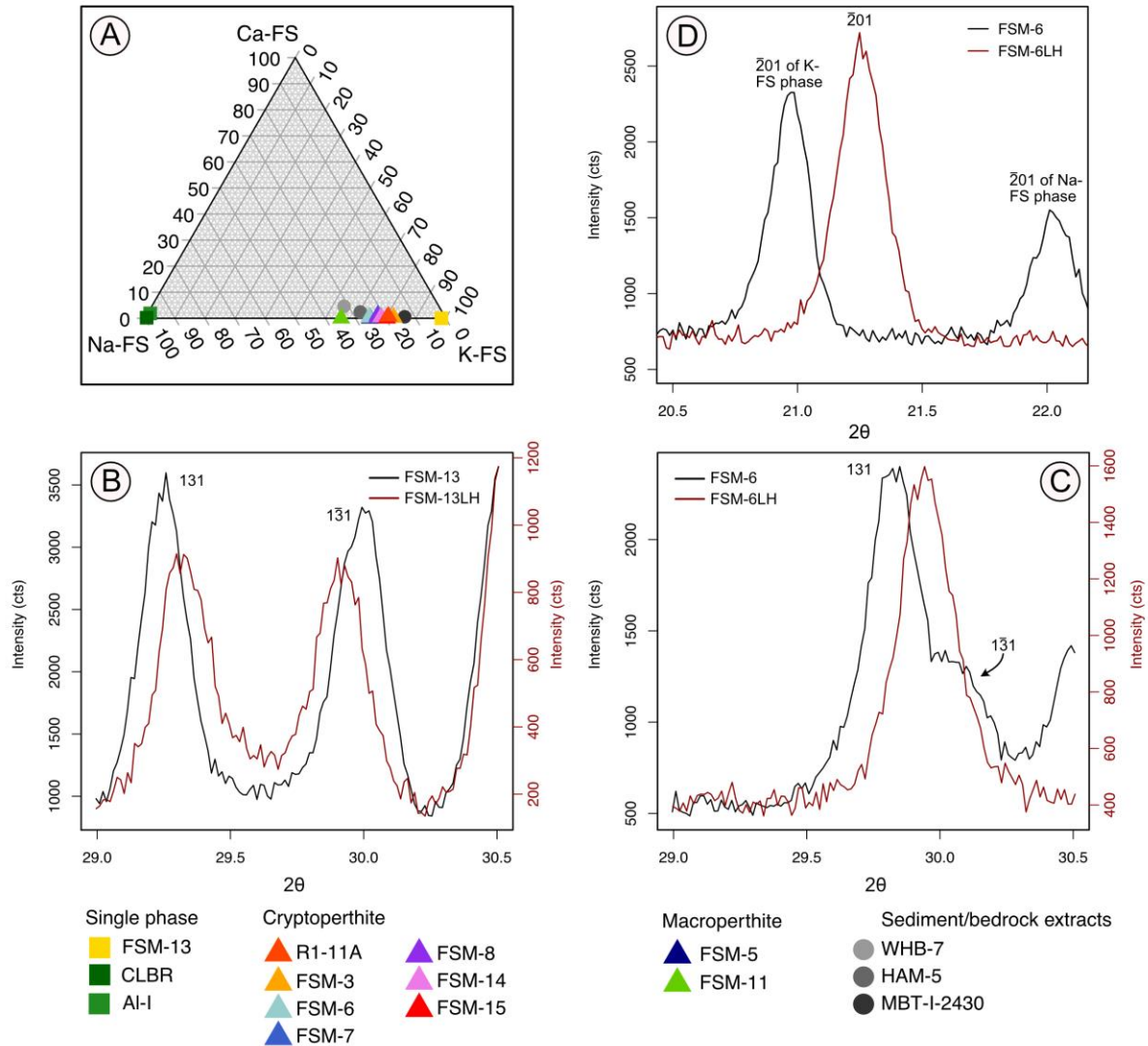
Fig. 1. A) Relative feldspar composition (%) of the samples. The relative compositions of K-, Na- and Ca-feldspar were calculated using stoichiometric conversion of XRF results. B) X-ray diffraction pattern of FSM-13 (black line) and FSM-13LH (red line) in the range of 29.0° 2θ to 30.5° 2θ. Visible are the (131) and (1$\bar{3}$1) diffraction maxima. These two diffraction maxima move closer together due to the heating of the sample material. C) X-ray diffraction pattern of FSM-6 (black line) and FSM-6LH (red line) in the range of 29.0° 2θ to 30.5° 2θ. For FSM-6 (black line) a prominent (131) diffraction maxima is visible in the figure, and in addition a minor peak, which is the remainder of the (1$\bar{3}$1) diffraction peak. After heating and rapidly cooling, only a single (131) diffraction peak remains in FSM-6LH (red line). This indicates that the original material of FSM-13 (black line in B) is more ordered than the starting material of FSM-6 (black line in C). For both samples, the X-ray diffraction pattern indicate the success of the heating experiment, as both samples are slightly more disordered than their starting material. However, it is expected that FSM-6LH is relatively more disordered than FSM-13LH. D) Comparison of the $\bar{2}$01 diffraction peak in perthite FSM-6 and in sanidine FSM-6LH. The heating experiment caused a homogenisation of the distribution of K$^+$ and Na$^+$ ions within the crystal. Whilst FSM-6 shows two $\bar{2}$01 diffraction peaks (on for each phase), FSM-6LH only shows a single diffraction peak, reflecting the homogeneous distribution of the cations. Radiation used in XRD analysis was Cu Kα.
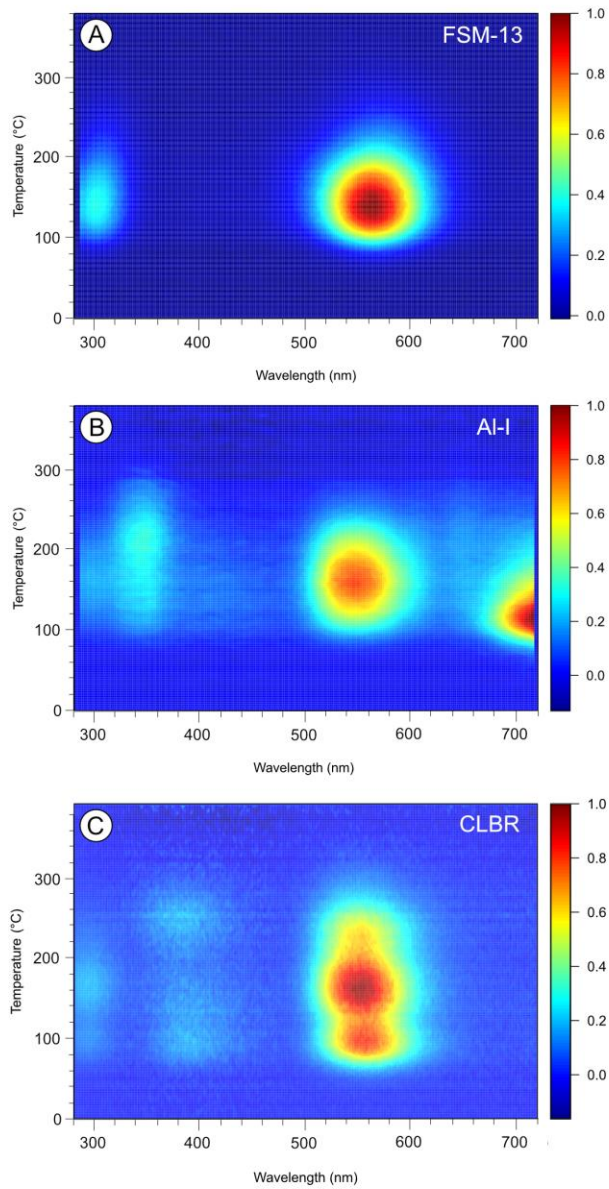
Fig. 2. TL emission spectra recorded up to 380 °C, from 280 to 720 nm. The samples shown in this figure are single-phase feldspar. FSM-13 is a microcline (A) and Al-I (B) and CLBR (C) are albite, with Al-I containing 5 % quartz. The TL intensities are normalised to the data point with the highest intensity.
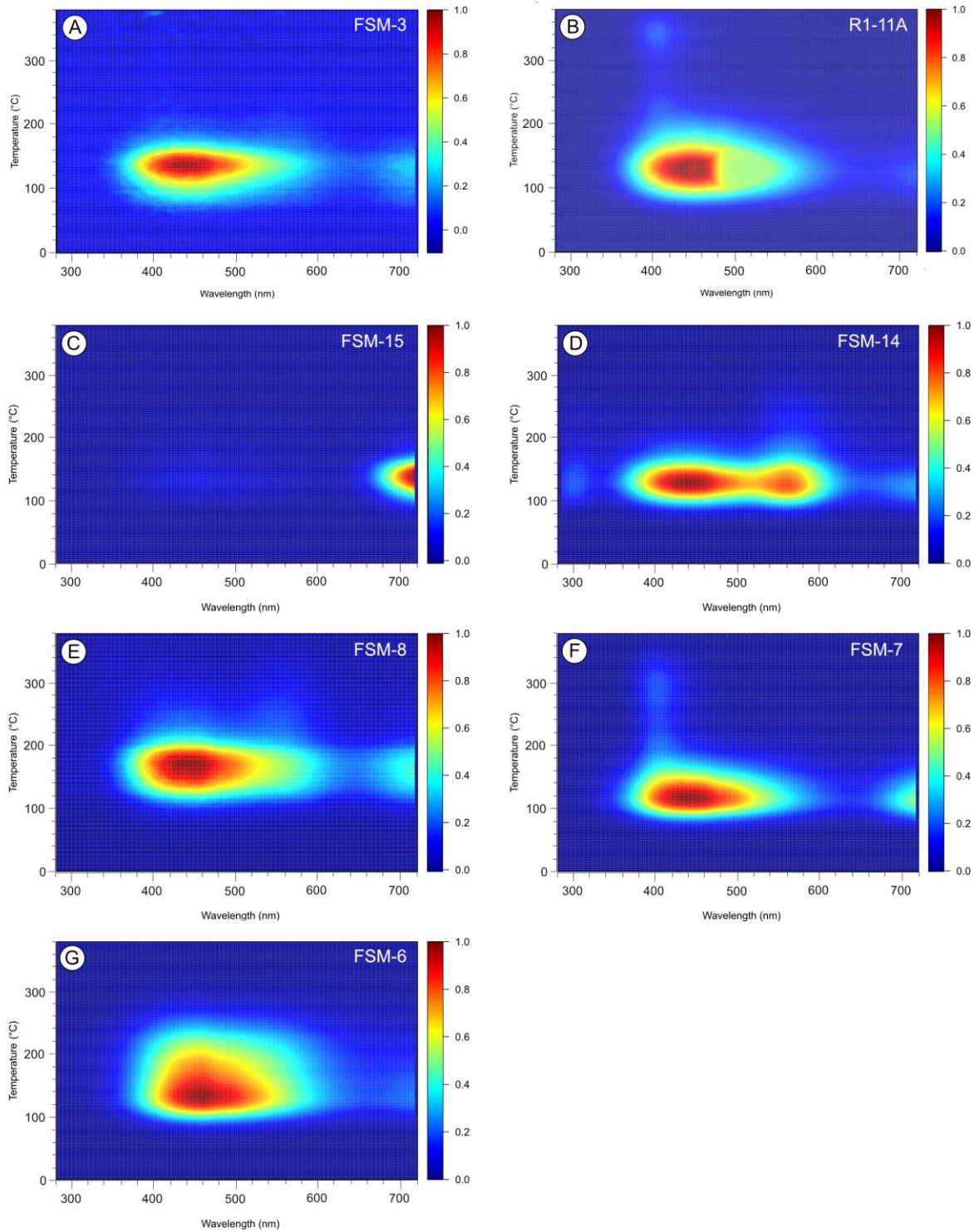
Fig. 3. TL emission spectra recorded up to 380 °C, from 280 to 720 nm. The samples shown in this figure are cryptoperthite: FSM-15 (C) is the only sample of the displayed samples, where Fe was detected during the XRF measurements. All samples consist of microcline and albite (A-F), except for FSM-6 (G), which consists of orthoclase and albite. The TL intensities are normalised to the data point with the highest intensity.
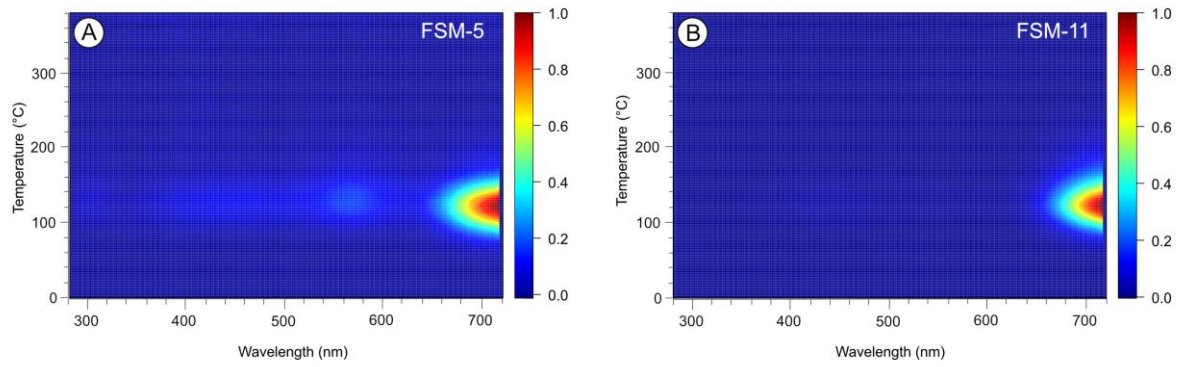
Fig. 4. TL emission spectra of perthites with coarse perthite lamella, visible with the naked eye: macroperthite. FSM-5 (A) is an amazonite sample, which shows twinning in the albite phase. XRF-measurements showed the presence of Fe in FSM-11 (B), which also is of orange colour in the microcline phase. The TL intensities are normalised to the data point with the highest intensity.
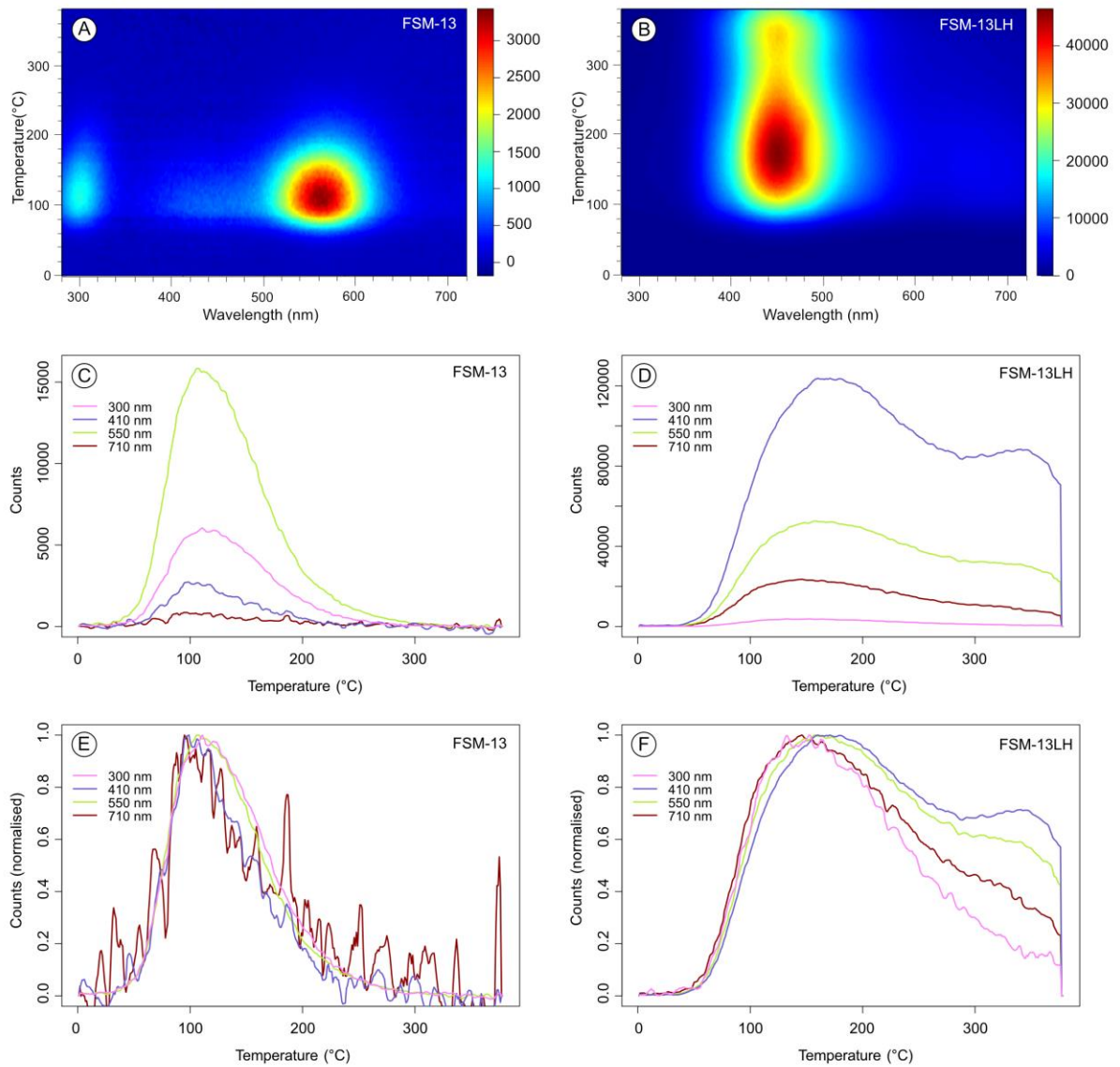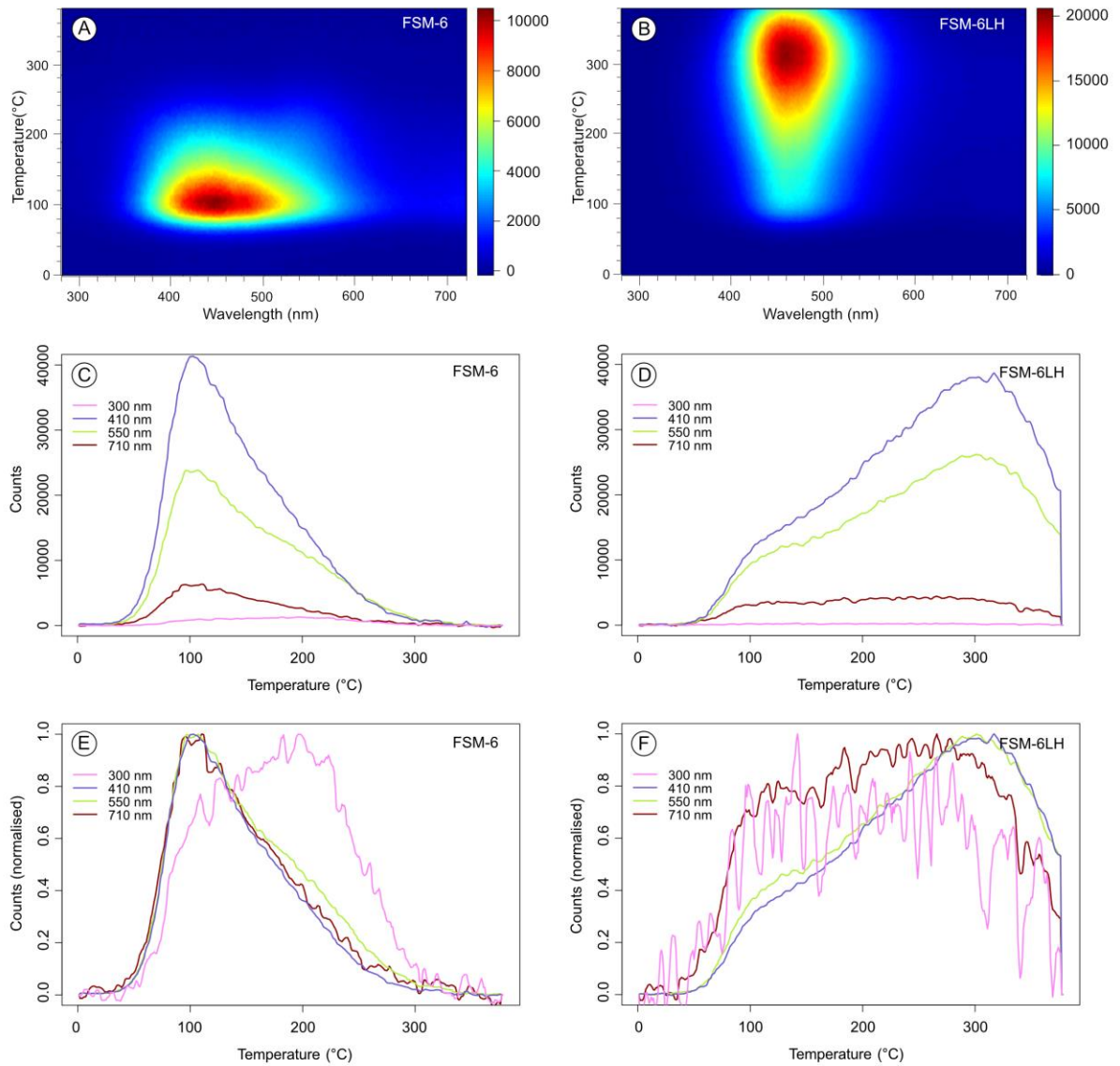
Fig. 5. Effect of heating sample FSM-13 (single phase microcline) at 1050 °C for 10 days. (A) TL spectra of the unheated material of FSM-13, (B) TL spectra of the heated fraction. (C) and (D) show the TL curve extracted from the TL spectra for different wavelengths for FSM-13 and FSM-13LH, respectively. (E) and (F) show the same data as (C) and (D), but normalised to the highest intensity for each TL curve. The measured intensities are absolute intensities in counts/0.4 nm/°C. For these measurements the same mass of sample material was used and the samples were measured during the same measurement sequence.

Fig. 6. Effect of heating sample FSM-6 (orthoclase and albite) at 1050 °C for 10 days. (A) TL spectra of the unheated material of FSM-6, (B) TL spectra of the heated fraction. (C) and (D) show the TL curve extracted from the TL spectra for different wavelengths for FSM-6 and FSM-6LH, respectively. (E) and (F) show the same data as (C) and (D), but normalised to the highest intensity for each TL curve. The measured intensities are absolute intensities (in cts/0.4 nm/°C). For these measurements the same mass of sample material was used and the samples were measured during the same measurement sequence.
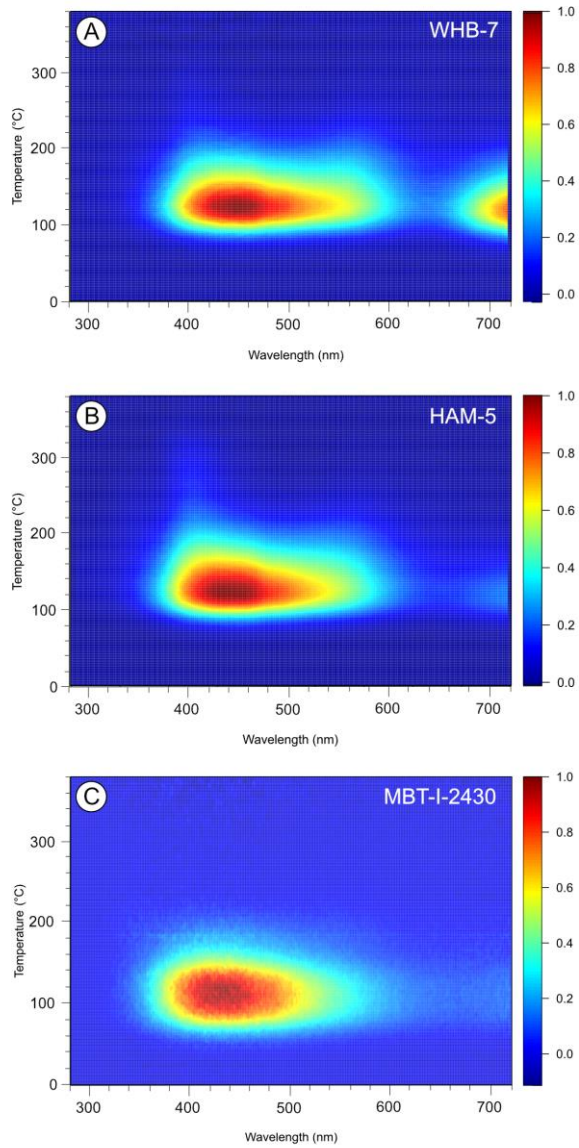
Fig. 7. TL emission spectra of alkali feldspars extracted from sediments (WHB-7, HAM-5) and bedrock (MBT-I-2430). The TL intensities are normalised to the data point with the highest intensity.
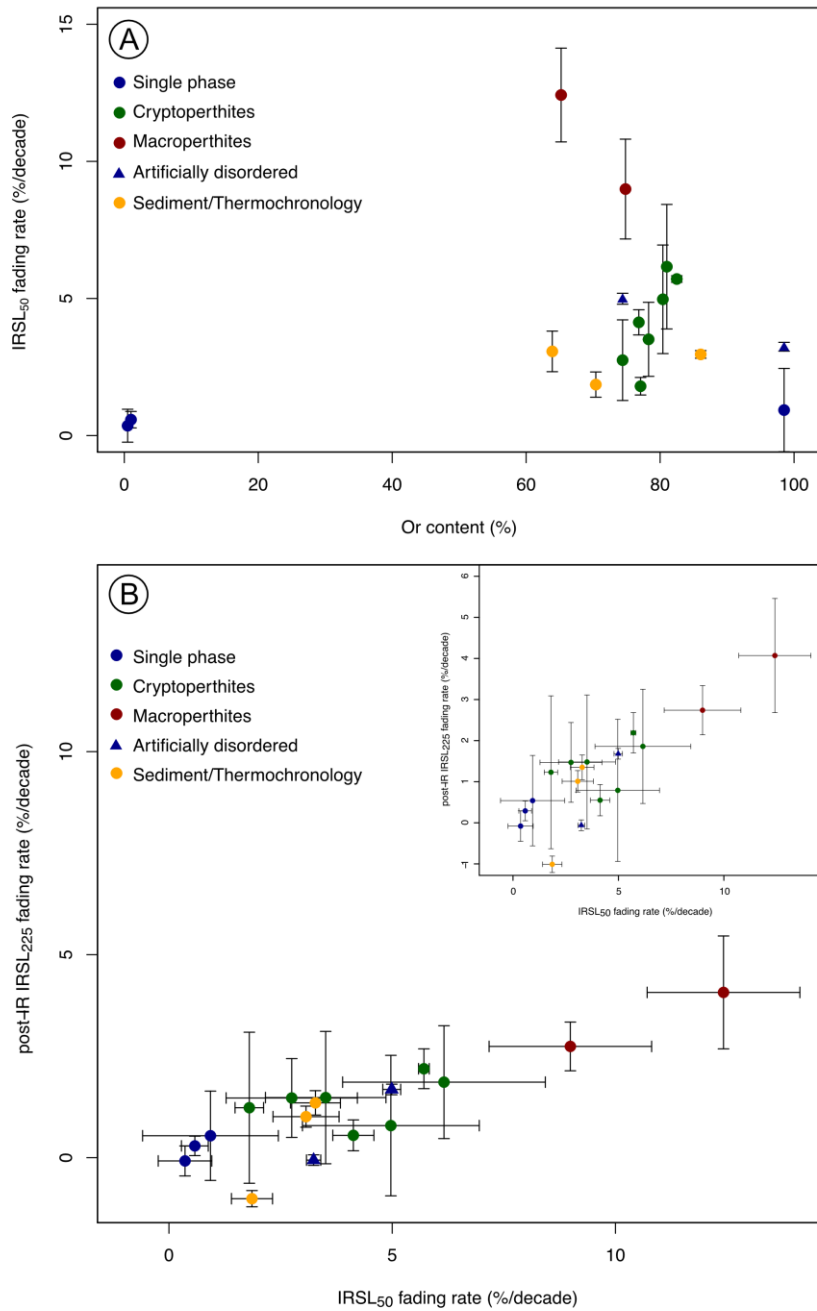
Fig. 8. A) Comparison of fading rates of the post-IR IRSL$_{225}$ signal and the IRSL$_{50}$ signal, obtained using the post-IRIRSL protocol. The inset is a close-up version of B. The data points in A and B are the average fading rate of the measured aliquots for each sample and the standard deviation of these measurements. B) Fading rates for the IRSL$_{50}$ signal measured using a post-IR$_{50}$IRSL$_{225}$ protocol, with a 250 °C preheat for 60 s.

Exploring sources of variation in thermoluminescence emissions and anomalous fading in alkali feldspars

Supplementary Material

S. Riedesel[1], A.M.T. Bell[2], G.A.T. Duller[1], A.A. Finch[3], M. Jain[4], G.E. King[5], N.J. Pearce[1], H. M. Roberts[1]

[1]Department of Geography and Earth Sciences, Aberystwyth University, United Kingdom

[2]Materials and Engineering Research Institute, Faculty of Science, Technology and Arts, Sheffield Hallam University, United Kingdom

[3]School of Earth and Environmental Sciences, University of St. Andrews, St. Andrews, United Kingdom

[4]Department of Physics, Technical University of Denmark, DTU Risø Campus, Roskilde, Denmark

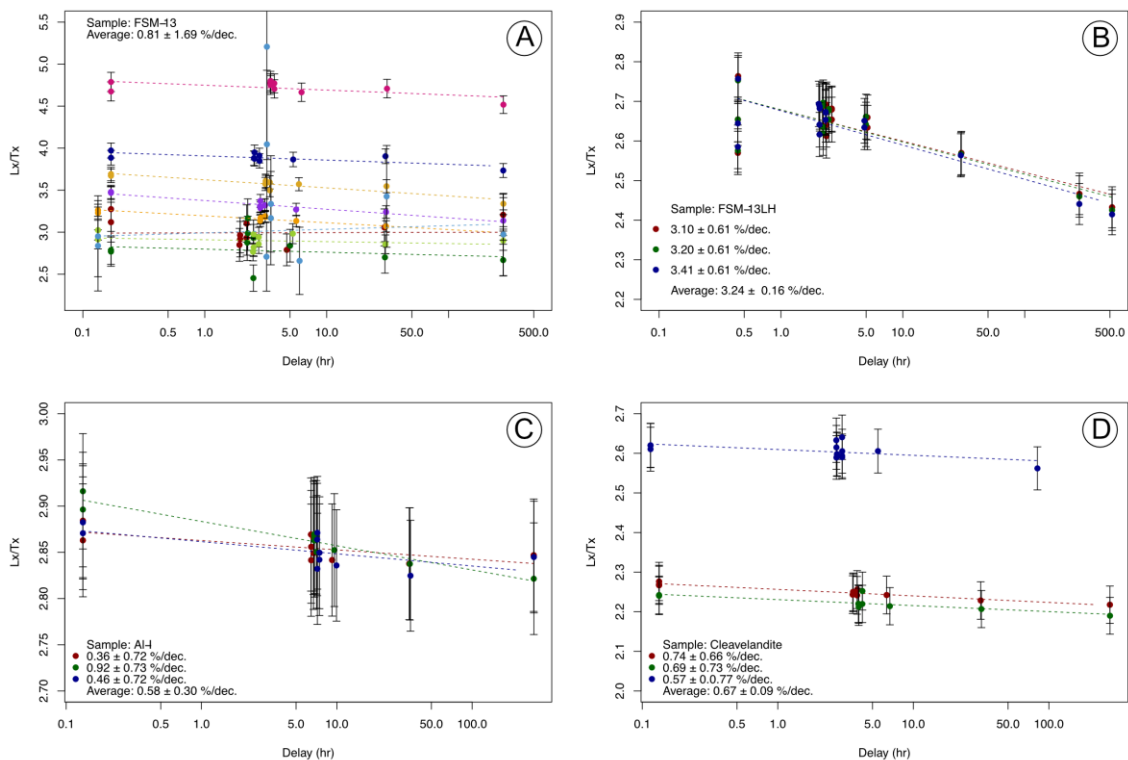[5]Institute of Earth Surface Dynamics, University of Lausanne, Lausanne, Switzerland

Figures

Fig. S1. Fading results as Lx/Tx versus delay time for FSM-13 (A), FSM-13LH (B), Al-I (C) and
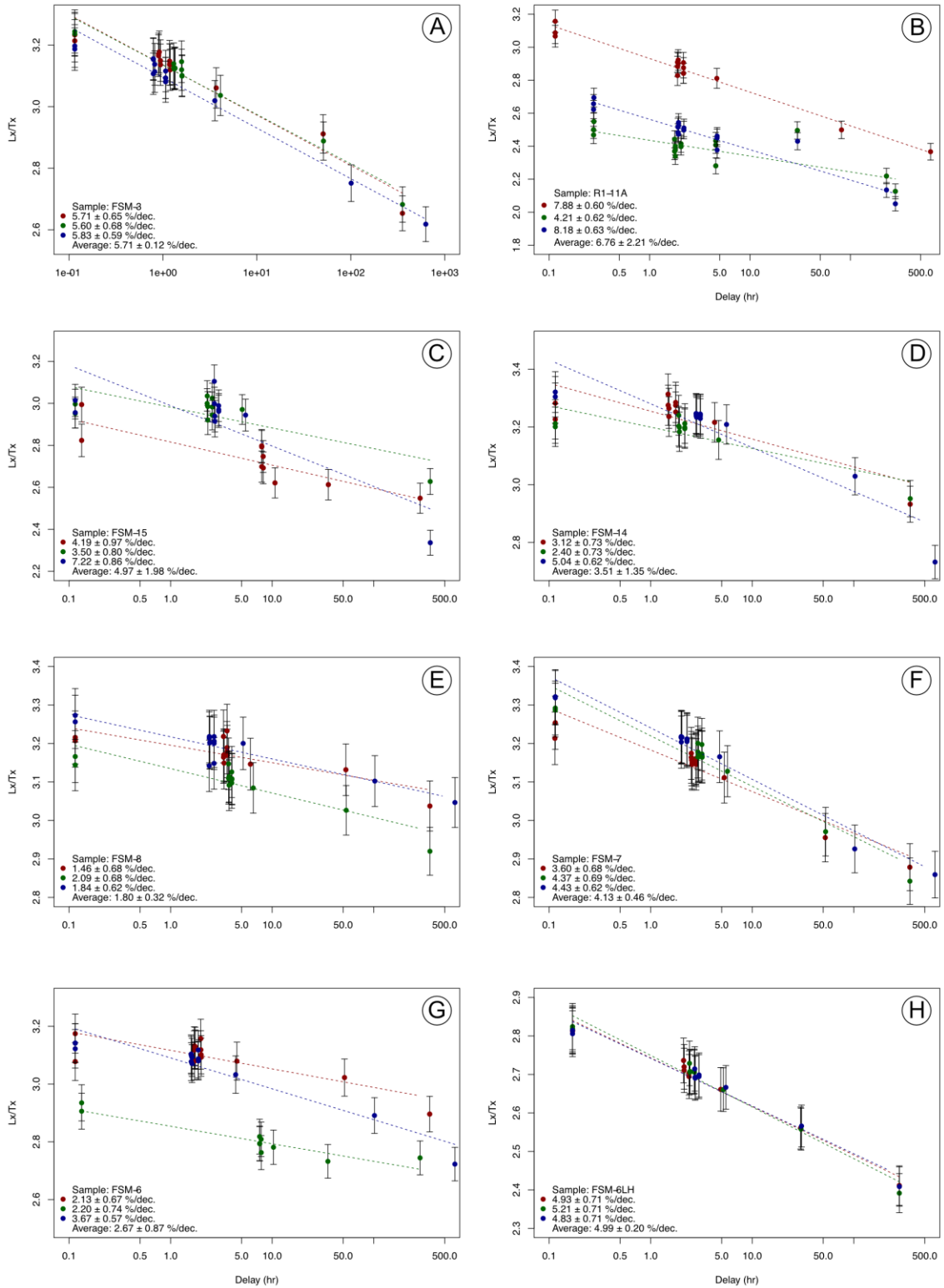Cleavelandite (D).

Fig. S2. Fading results as Lx/Tx versus delay time for FSM-3 (A), R1-11A (B), FSM-15 (C) FSM-14 (D), FSM-8 (E), FSM-7 (F), FSM-6 (G) and FSM-6LH (H).
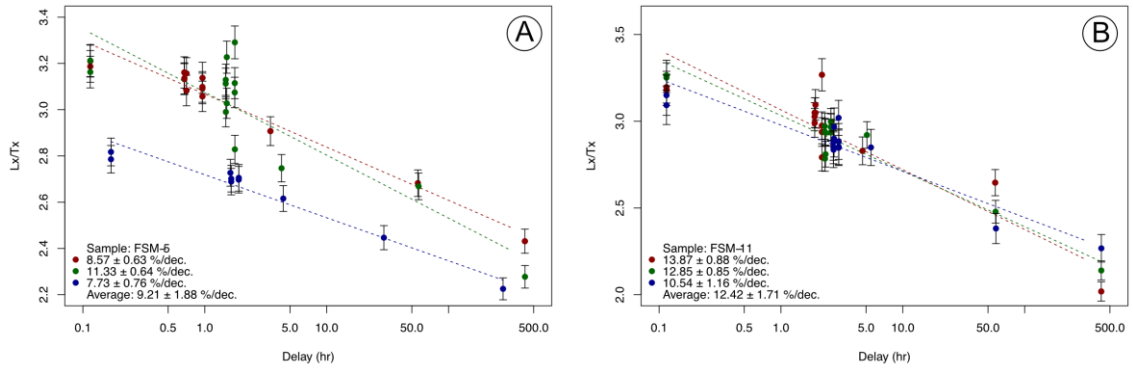

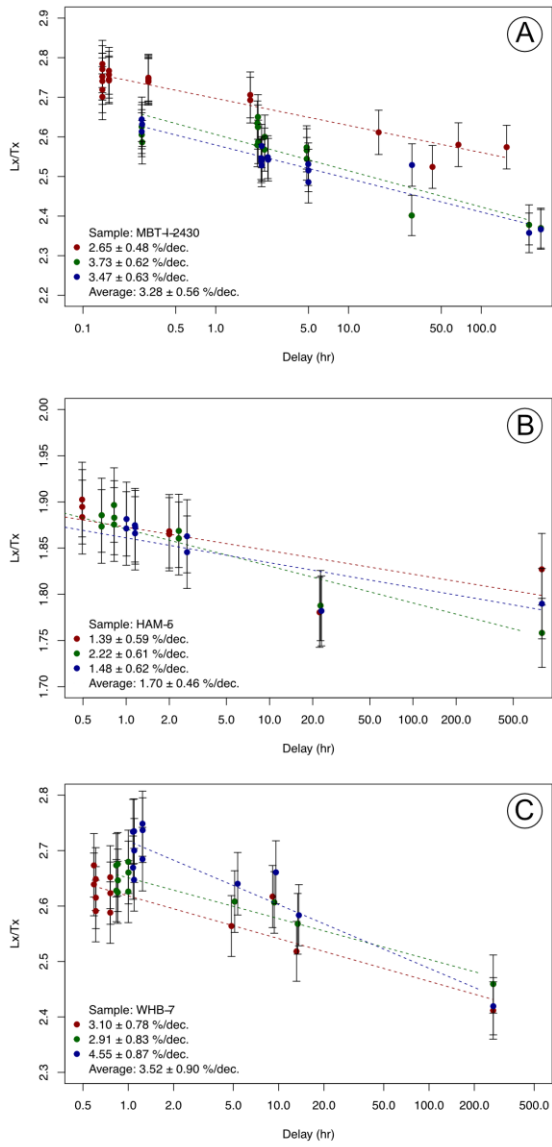Fig. S3. Fading results as Lx/Tx versus delay time (hours) for FSM-5 (A) and FSM-11 (B).

Fig. S4. Fading results as Lx/Tx versus delay time (in hours) for MBT-I-2430 (A), HAM-5 (B) and WHB-7 (C).

Tables

Table S1. Semi-quantitative XRF results (wt%)of samples used in this study, except R1-11A and Cleavelandite.

Oxide	HAM-5	241_WHB-7kf	MBT-I-2430	255_FSM-3	255_FSM-5	255_FSM-6	255_FSM-7	255_FSM-8	255_FSM-11	255_FSM-13	255_FSM-14	255_FSM-15
Al_2O_3	33.80 ± 0.50	20.20 ± 0.60	22.10 ± 0.40	23.50 ± 1.00	21.30 ± 0.50	23.20 ± 1.00	21.20 ± 0.50	25.60 ± 2.00	20.00 ± 0.40	22.00 ± 0.30	21.80 ± 1.00	21.80 ± 1.00
SiO_2	46.00 ± 0.40	65.90 ± 3.00	63.20 ± 2.00	61.40 ± 2.00	62.50 ± 2.00	62.70 ± 0.40	62.80 ± 2.00	55.60 ± 0.60	64.30 ± 2.00	62.00 ± 2.00	61.90 ± 2.00	63.10 ± 2.00
K_2O	14.40 ± 0.10	8.38 ± 0.10	13.00 ± 0.10	13.20 ± 0.10	13.10 ± 0.10	11.10 ± 0.10	12.70 ± 0.10	15.20 ± 0.10	11.20 ± 0.10	15.70 ± 0.10	12.00 ± 0.10	12.60 ± 0.10
Na_2O	3.66 ± 0.20	2.72 ± 0.30	1.33 ± 0.10	1.81 ± 0.10	2.90 ± 0.20.	2.48 ± 0.10	2.39 ± 0.20	2.93 ± 0.20	3.93 ± 0.20	0.16 ± 0.03	2.14 ± 0.10	2.02 ± 0.10
CaO	0.59 ± 0.03	0.72 ± 0.04	0.10 ± 0.01	0.06 ± 0.01	0.00 ± 0.00	0.06 ± 0.01	0.24 ± 0.02	0.08 ± 0.01	0.00 ± 0.00	0.00 ± 0.00	0.09 ± 0.01	0.00 ± 0.00
Fe_2O_3	0.40 ± 0.02	1.23 ± 0.03	0.00 ± 0.00	0.00 ± 0.00	0.00 ± 0.00	0.00 ± 0.00	0.00 ± 0.00	0.00 ± 0.00	0.46 ± 0.02	0.00 ± 0.0	0.00 ± 0.00	0.17 ± 0.01
TiO_2	0.14 ± 0.01	0.02 ± 0.00	0.00 ± 0.00	0.00 ± 0.00	0.00 ± 0.00	0.00 ± 0.00	0.00 ± 0.00	0.00 ± 0.00	0.00 ± 0.00	0.00 ± 0.00	0.00 ± 0.00	0.00 ± 0.00
MgO	0.47 ± 0.04	0.59 ± 0.07	0.00 ± 0.00	0.00 ± 0.00	0.00 ± 0.00	0.00 ± 0.00	0.00 ± 0.00	0.00 ± 0.00	0.00 ± 0.00	0.00 ± 0.0	0.00 ± 0.00	0.00 ± 0.00
Other	0.45 ± 0.02	0.29 ± 0.09	0.21 ± 0.01	0.07 ± 0.00	0.12 ± 0.01	0.40 ± 0.02	0.61 ± 0.02	0.62 ± 0.13	0.19 ± 0.01	0.18 ± 0.00	2.15 ± 0.12	0.26 ± 0.01